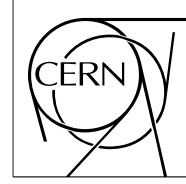


The Compact Muon Solenoid Experiment

Analysis Note

The content of this note is intended for CMS internal use and distribution only



04 November 2010

Angular Analysis of Resonances $pp \rightarrow X \rightarrow ZZ$

A. Bonato, A.V. Gritsan, Z.J. Guo, N.V. Tran, A. Whitbeck
Johns Hopkins University, Baltimore, MD, USA

Abstract

If a new resonance is found in the $X \rightarrow ZZ$ channel, the question will be to identify its nature and origin. While one possibility is the Standard Model Higgs boson which is a scalar, a wide range of other possible new particles with the same signature is possible, such as a pseudoscalar or a non-SM Higgs scalar, a vector or axial-vector (new gauge boson), or a tensor (Kaluza-Klein excitation of the graviton, hidden glueball) particle. We use a multivariate likelihood fit which includes full angular and kinematic information in the decay chain. This allows one to distinguish between various signal quantum numbers and coupling constants to SM fields in a model-independent way. This approach also improves signal over background separation. In addition to the golden four-lepton final state, we investigate the semi-leptonic final state with two jets and show that, at higher mass, this channel will dominate measurements of the $X \rightarrow ZZ$ decay and both channels allow full angular analysis of the final state. The implementation in the `Roofit` package allows combination with other statistical tools developed on CMS and other LHC experiments. A dedicated MC program is used to simulate various types of signal including all spin correlations. Detailed MC studies are performed with several bench-mark processes and several mass assumptions. Emphasis is given to the scenario for the first LHC run with 1/fb at 7 TeV center-of-mass energy.

Contents

1	Introduction	3
2	Expectation for the $X \rightarrow ZZ$ Resonances	4
3	Simulation, Reconstruction, and Selection	9
3.1	Reconstruction of $X \rightarrow ZZ \rightarrow 4l$	9
3.2	Reconstruction of $X \rightarrow ZZ \rightarrow 2l2j$	11
3.3	Expected reconstructed yields	12
4	Analysis Techniques	15
4.1	Parameterization of the probability density functions	15
4.2	Parameterization of the signal angular distributions: lepton channels	15
4.3	Parameterization of background angular distributions: lepton channels	16
4.4	Parameterization of angular distributions: channels with jets	17
4.5	Parameterization of the invariant mass distributions	18
4.6	Parameterization below the ZZ threshold	19
4.7	Validation and study techniques	19
5	Results	25
6	Analysis of the First ZZ Event	30
7	Summary and Discussion	31
8	Acknowledgements	32
A	Angular Formalism	32
B	Mass Distributions Below the ZZ Threshold	33

1 Introduction

The Standard Model (SM) of fundamental particles points to a component of empty space, the Higgs field, which gives elementary particles the property of mass. However, the undiscovered symmetries of nature which unify the fundamental forces and particles, the puzzle of dark matter and energy, and the apparent lack of antimatter in our Universe, all these mysteries point to physics Beyond the Standard Model (BSM). It is expected that the Large Hadron Collider will either produce evidence for physics BSM or confirm the SM within its energy reach. In either case, making a discovery or setting a limit on the production of a SM Higgs boson, a manifestation of the Higgs field, would be a priority.

Current precision tests of the Standard Model [1] set limits on the Higgs mass but a mass window of up to ~ 200 GeV is still open. Moreover, there are internal inconsistencies in complementary constraints and looking for a Standard-Model-like Higgs boson above 200 GeV is still prevalent. For a mass above 120 GeV, the channel $H \rightarrow ZZ^{(*)} \rightarrow 4l^{\pm}$ becomes important. It dominates the discovery potential of the Standard Model Higgs decay above the ZZ mass threshold and competes with the $H \rightarrow \gamma\gamma$ channels below the ZZ mass threshold. Moreover, little is studied about the final state with jets $H \rightarrow ZZ^{(*)} \rightarrow 2l2j$ while it may dominate sensitivity of the ZZ final state at higher masses.

The Standard Model Higgs boson is a scalar, but the same signature may be an evidence for a pseudoscalar, vector (gauge boson), or tensor particle (Kaluza-Klein excitations of the graviton, hidden glueball in hidden valley theories). Distinguishing between different possibilities in a broad range of masses is important. If a Higgs-like object is found on LHC, the question will be to identify its nature and origin. Full angular analysis of its decay products will be an important (and sometimes the only) way to understand it and distinguish between the SM Higgs and something different. Unique results could be obtained with such a channel. Alternatively, if no Higgs-like object is found, then using angular variables could help one to separate background and set tighter limits on the signal.

The angular distributions of the Higgs decay to ZZ have been studied in the literature [2, 3, 4, 5, 6, 7, 8, 9]. However, only recently the complete treatment of production and decay kinematics in the case of the most general spin and couplings was shown in Ref. [10], with similar work following in Ref. [11].

In Fig. 1 we illustrate the angular distribution in the production and decay chain $ab \rightarrow X \rightarrow P_1 P_2 \rightarrow p_{11} p_{12} p_{21} p_{22}$ with an example of the $ab \rightarrow X \rightarrow ZZ \rightarrow 4l$ or $2l2q$ (where quarks q hadronize to jets, which we refer to as $2l2j$ channel later) chain with two partons a and b , such as gg or $q\bar{q}$. The angular distribution can be expressed as a function of three helicity angles θ_1 , θ_2 , and Φ , and two production angles θ^* and Ψ , as shown in Fig. 1. An equivalent set of variables is sometimes used, as also illustrated on the right plot of Fig. 1: $(\theta_1, \theta_2, \Phi, \theta^*, \Phi_1)$,

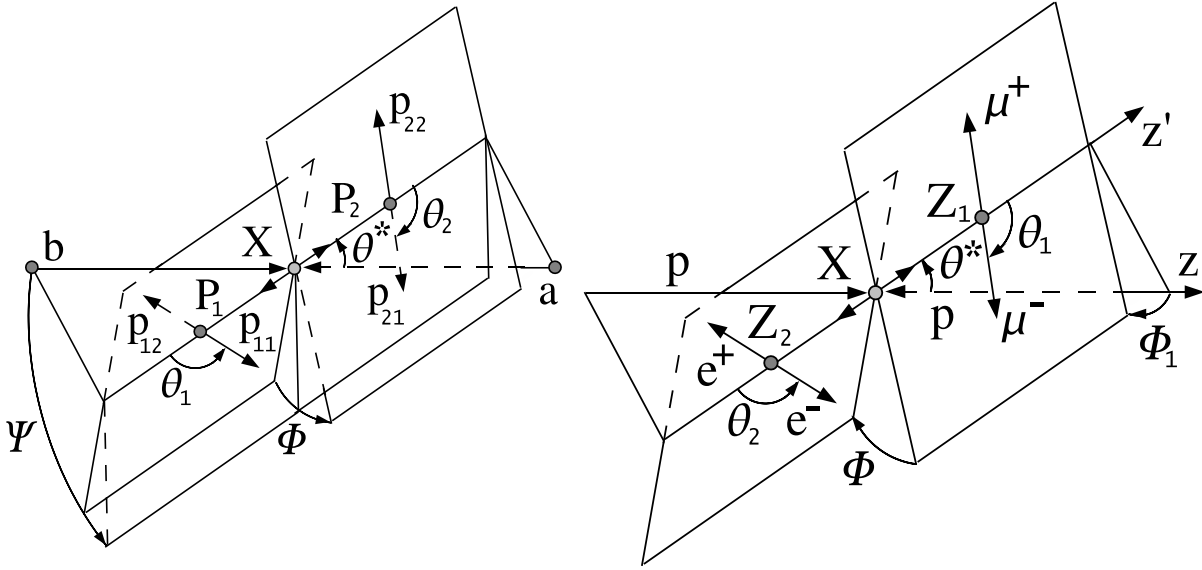


Figure 1: Left: Illustration of an exotic X particle production and decay $ab \rightarrow X \rightarrow P_1 P_2 \rightarrow p_{11} p_{12} p_{21} p_{22}$ with the two production angles θ^* and Ψ shown in the X rest frame and three decay angles θ_1 , θ_2 , and Φ shown in the P_i rest frames. Right: an equivalent definition of angles, where one production angle is redefined as $\Psi = \Phi_1 + \Phi/2$.

where $\Psi = \Phi_1 + \Phi/2$.

Here θ_i is the angle between the direction of the l^- or q from the $Z \rightarrow l^+l^-$ or $q\bar{q}$ (where the quark-antiquark pair produces two jets) and the direction opposite the X in the Z rest frame, and Φ is the angle between the decay planes of the two Z systems. The two Z 's are distinguished by their decay type or, in case their daughters are the same type of particles, by an arbitrary convention. The production angle θ^* is defined as the angle between the parton collision axis z and the X decay axis in the X rest frame. The fifth angle can be defined as the angle between the production plane and the average between the two decay planes shown in Fig. 1. Two other equivalent angles Φ_1 and Φ_2 could be defined as the angles between the production plane and one of the Z decay planes. However, these angles are not independent from Φ and Ψ , as $\Phi = \Phi_2 - \Phi_1$ and $\Psi = \Phi_1 + \Phi/2$. Sometimes it may be convenient to use the (Φ, Φ_1) combination instead of (Φ, Ψ) .

The differential decay width has in general nine complex amplitudes $A_{\lambda_1\lambda_2}$ corresponding to the spin projection of the Z bosons, where the possible helicity values are $\lambda_i = 0$ or ± 1 . In general, nine spin configurations are possible for the spin projection on its direction (helicity) of each of the two Z bosons (3×3). However, the number of independent configurations is reduced to six when the two X decay daughters are identical particles, such as ZZ , where, for example, $A_{\lambda_1\lambda_2}$ and $A_{\lambda_2\lambda_1}$ describe the same physical case,

$$A_{\lambda_1\lambda_2} = (-1)^J A_{\lambda_2\lambda_1}, \quad (1)$$

while if parity is conserved, further constraints apply [12, 13]

$$A_{\lambda_1\lambda_2} = \eta_P (-1)^J A_{-\lambda_1-\lambda_2}, \quad (2)$$

where η_P is the parity of the X particle.

For a spin-zero X particle, only $\lambda_1 - \lambda_2 = 0$ values are possible. Therefore only A_{++} , A_{--} , and A_{00} contribute. For a spin-one X particle, $|\lambda_1 - \lambda_2| \leq 1$ and A_{+-} and A_{-+} are not possible. In addition, Bose symmetry prohibits A_{++} , A_{--} , and A_{00} amplitudes. Moreover, the X resonance can be produced in different spin polarization states, depending on its spin. For a spin-two X in general all five spin projections on the z axis are possible. For a spin-one resonance, only spin-one projections are possible if chiral symmetry is exact. Spin one projection can be produced in $q\bar{q} \rightarrow X$, while spin zero or two projections are created in gluon fusion $gg \rightarrow X$. Since each decay amplitude and spin state corresponds to a unique angular distribution, we can use this to distinguish different hypotheses, as we discuss in the following sections.

The angular analysis formalism is discussed in detail in Ref. [10] and the main angular formulas are given in Appendix A. The issues specific to mass distributions below the ZZ threshold are discussed in Appendix B.

2 Expectation for the $X \rightarrow ZZ$ Resonances

As discussed in Sec. 1, the angular analysis of ZZ decay products would allow one to distinguish between various possible signals at the LHC. Here, we further discuss the feasibility of these various signal resonances and the expectations for what one may observe based on theoretical considerations.

The SM Higgs case is well-explored. The $H \rightarrow ZZ \rightarrow 4l^\pm$ process becomes important for masses of the Higgs boson above 120 GeV. The cross-section for the SM Higgs to ZZ is 4 – 50 fb depending on the mass where the upper limit on the mass range is constrained by unitarity at ~ 800 GeV. In the following sections, we use the SM Higgs case as the baseline for comparing the different scenarios.

There are plausible models for a spin-1 particle decaying to the ZZ final state [14]. All spin states are in principle possible in the models with hidden valleys, where hidden glueballs are composite states [15]. In the case of the spin-2 exotic particle, we consider a particularly interesting scenario, the Randall-Sundrum (RS) model which predicts a tower of spin-2 Kaluza-Klein gravitons [16]. The masses for the graviton states are:

$$m_n = kx_n e^{kr_c\pi} \quad (3)$$

where $c = k/M_{pl}$ gives the scale of the model, M_{pl} is the reduced Planck mass, r_c is the compactification radius of the model, and x_n are the roots of the Bessel function and only the 0th root is considered. The values of the c usually considered in the literature range from 0.01 to 0.1, though $c \sim 1$ may be still theoretically possible [17]. In the case of the classic RS1 model at the LHC, other channels such as $\gamma\gamma$ [18], l^+l^- [19, 20], and $t\bar{t}$ [21] may dominate. However, in modified RS models which address the flavor problem, the SM particles are localized in

the bulk [17], and therefore decays to light fermions and photons are highly suppressed. In these cases, decays to ZZ may become the dominant discovery channels, depending on the mass range, like for the SM Higgs.

In Fig. 2, the product of particle X production cross-section (at LHC energy of 7 TeV) and the branching fraction $X \rightarrow ZZ$ is shown for several scenarios of RS Graviton, SM Higgs, and an effective Tevatron limit. The expected $G \rightarrow ZZ$ yield depends on the value of c . The Tevatron limit set by CDF [22] at $m_G > 500$ GeV for $c = 0.1$.

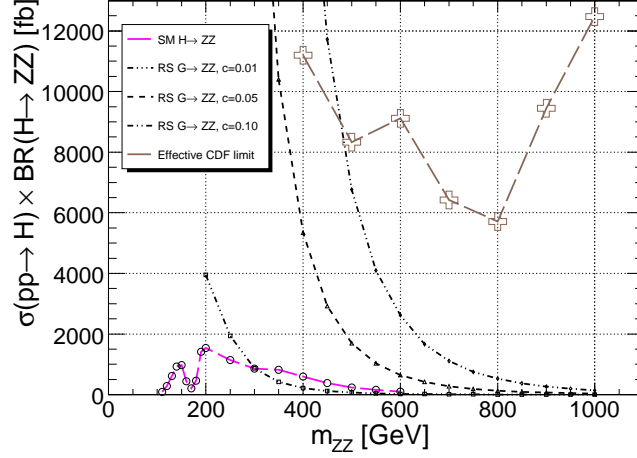


Figure 2: The product of particle X production cross-section (at LHC energy of 7 TeV) and the branching fraction $X \rightarrow ZZ$ for four scenarios: SM Higgs and RS graviton with $c = 0.01, 0.50, 0.10$. Effective limit extracted from CDF results with 2.9/fb of data is shown with crosses, which is recalculated from the limits on the RS Graviton with $c = 0.10$ production at Tevatron.

With the first LHC run expected to collect 1/fb of data with an LHC energy of 7 TeV, there will be either improved limits or even observation of a new state depending on the model parameters. We take the first LHC run with 1/fb of data as a baseline for analysis in this note. We consider two scenarios:

- scenario A (“pessimistic”): no signal, only background events contribute and upper limit is calculated;
- scenario B (“optimistic”): maximum signal observed, which is still consistent with the CDF limit, which corresponds to about 20 signal events in the channel $G \rightarrow ZZ \rightarrow 4l$.

The above two scenarios target either SM Higgs exclusion (scenario A) or an exotic signal which is not ruled out by the current Tevatron data (scenario B). The latter scenario is considered to show the power of the angular information to separate various spin and coupling constant hypotheses. In the former scenario we still illustrate the power of angular (kinematic) variables to suppress background.

If only the golden final states $ZZ \rightarrow \mu^+\mu^-\mu^+\mu^-$, $\mu^+\mu^-e^+e^-$, and $e^+e^-e^+e^-$ are considered, there is a price to pay in low branching fraction of the lepton final state $Z \rightarrow l^+l^-$ of only about 6.7%. On the other hand, the hadron final state of the Z decay is close to 70%. Therefore, in addition to the fully leptonic final state we consider the semi-leptonic final state when one Z decays to two hadronic jets and the other Z decays to two leptons. Higher backgrounds and worse energy resolution are expected for the final state with jets, but this is offset by more than a factor of ten larger signal yield, which could make this the dominant channel at higher invariant masses. In addition, the final state with one Z decaying to charged leptons $Z \rightarrow l^+l^-$ and the other Z decaying to neutrinos $Z \rightarrow \nu\bar{\nu}$ may be a good channel to improve sensitivity to signal at higher masses. However, we do not consider this final state for two reasons. First, this final state does not allow detailed polarization measurements and only the overall yield may be studied. Second, we still expect the final state with jets, $Z \rightarrow \text{hadrons}$ (branching $\sim 70\%$), to have larger rate than $Z \rightarrow \text{invisible}$ (branching $\sim 20\%$); and therefore, it has better sensitivity when the background is not too high (which is the case at higher mass with few/fb).

While there is a continuum spectrum of possible models of a resonance production and decay, corresponding to a continuum spectrum of possible contributing amplitudes, or equivalently coupling constants, we pick seven scenarios to illustrate the analysis techniques. These scenarios follow those suggested in Ref. [10] and are summarized in Table 1. The parameters of the seven models are summarized in Tables 2, 3, and 4. Projections

Table 1: The list of scenarios chosen for the analysis of the production and decay of an exotic X particle with quantum numbers J^P , following convention in Ref. [10]. For the two 2^+ cases, the superscripts m (minimal) and L (longitudinal) distinguish two scenarios, as discussed in the last column. When relevant, the relative fraction of $q\bar{q}$ production is taken to be 0 at $m_X = 250$ GeV, 0.15 at $m_X = 500$ GeV, and 0.25 at $m_X = 1$ TeV.

scenario (J^P)	X production	comments
0^+	$gg \rightarrow X$	SM Higgs-like scalar
0^-	$gg \rightarrow X$	pseudo-scalar
1^+	$q\bar{q} \rightarrow X$	exotic pseudo-vector
1^-	$q\bar{q} \rightarrow X$	exotic vector
2_m^+	gg and $q\bar{q} \rightarrow X$	Graviton-like tensor with minimal couplings
2_L^+	gg and $q\bar{q} \rightarrow X$	Graviton-like tensor longitudinally polarized and with $J_z = 0$ contribution
2^-	gg and $q\bar{q} \rightarrow X$	“pseudo-tensor”

of the ideal angular distributions (at generator level) for the seven signal scenarios and for the dominant background in the $4l$ channel are illustrated in Fig. 3. The polarization fractions are defined in Ref. [10] as follows $f_{\lambda_1\lambda_2} = |A_{\lambda_1\lambda_2}|^2 / \sum_{k,l=\pm,0} |A_{kl}|^2$, $\phi_{\lambda_1\lambda_2} = \arg(A_{\lambda_1\lambda_2}/A_{00})$, and f_m are the fractions of the initial state spin projection m on the z axis, with $f_{\pm 1} = f_{z1}/2$, $f_{\pm 2} = f_{z2}/2$, and $f_0 = f_{z0} = (1 - f_{z1} - f_{z2})$. Only nonzero and primary parameters are quoted in the Tables, while other parameters can be deduced from the relationship of amplitudes. When the X decays to two identical particles and parity is conserved, the following relationships hold, following Eqs. (1) and (2). For 0^+ , A_{00} and $A_{++} = A_{--}$ are nonzero. For 0^- , only $A_{++} = -A_{--}$ are nonzero. In the vector case $J^P = 1^-$, one has $A_{+0} = A_{-0} = -A_{0+} = -A_{0-}$, and for an axial vector $J^P = 1^+$ the amplitudes are related as $A_{+0} = -A_{-0} = -A_{0+} = A_{0-}$. For $J^P = 2^+$, A_{00} , $A_{++} = A_{--}$, $A_{+-} = A_{-+}$, and $A_{+0} = A_{0+} = A_{-0} = A_{0-}$ are nonzero. For $J^P = 2^-$, $A_{++} = -A_{--}$ and $A_{+0} = A_{0+} = -A_{-0} = -A_{0-}$ contribute. Therefore, $f_{++} = f_{--}$, $f_{+-} = f_{-+}$, and $f_{+0} = f_{0+} = f_{-0} = f_{0-}$.

In this note, we study the above seven scenarios at four values of the X resonance mass: 140 GeV, 250 GeV, 500 GeV, and 1000 GeV. Moreover, the angular formalism is applicable directly to the case of a resonance produced below the ZZ mass threshold, that is with $m_X < 2m_Z$, as discussed in Appendix B. Therefore we consider one additional mass point at $m_X = 140$ GeV. In the latter case the amplitude decomposition is not well-defined because amplitude fractions depend on the invariant mass of the virtual Z^* . In this case we consider two scenarios 0^+ and 0^- , which correspond to $a_1 \neq 0$ and $a_3 \neq 0$ in Eq. (8) of Appendix A, respectively. As mentioned above, all studies are performed assuming 1/fb of data with LHC energy of 7 TeV for both signal yield scenarios (optimistic and pessimistic).

Table 2: Polarization parameters describing 0^+ and 0^- models with SM Higgs-like scalar X (0^+) and pseudoscalar (0^-), as discussed in Table 1. Three masses of X are considered.

	$m_X = 250 \text{ GeV}$		$m_X = 500 \text{ GeV}$		$m_X = 1 \text{ TeV}$	
	0^+	0^-	0^+	0^-	0^+	0^-
f_{00}	0.792	–	0.990	–	1.000	–
f_{++}	0.104	0.500	0.005	0.500	0.000	0.500
f_{--}	0.104	0.500	0.005	0.500	0.000	0.500
ϕ_{++}	π	π	π	π	π	π
ϕ_{--}	π	0	π	0	π	0

Table 3: Polarization parameters describing 1^+ and 1^- models with pseudovector X (0^+) and vector (1^-), as discussed in Table 1. Three masses of X are considered.

	$m_X = 250 \text{ GeV}$		$m_X = 500 \text{ GeV}$		$m_X = 1 \text{ TeV}$	
	1^+	1^-	1^+	1^-	1^+	1^-
f_{+0}	0.250	0.250	0.250	0.250	0.250	0.250
$(\phi_{+0} - \phi_{0-})$	0	π	0	π	0	π

Table 4: Polarization parameters describing 2_m^+ , 2_L^+ , and 2^- models, as discussed in Table 1. Three masses of X are considered.

	$m_X = 250 \text{ GeV}$			$m_X = 500 \text{ GeV}$			$m_X = 1 \text{ TeV}$		
	2_m^+	2_L^+	2^-	2_m^+	2_L^+	2^-	2_m^+	2_L^+	2^-
f_{z0}	0.000	0.600	0.000	0.000	0.510	0.000	0.000	0.450	0.000
f_{z1}	0.000	0.000	0.000	0.150	0.150	0.150	0.250	0.250	0.250
f_{z2}	1.000	0.400	1.000	0.850	0.340	0.850	0.750	0.300	0.750
f_{00}	0.110	0.792	–	0.086	0.990	–	0.110	1.000	–
f_{++}	0.013	0.104	0.125	0.001	0.005	0.026	0.000	0.000	0.000
f_{+-}	0.282	0.000	–	0.402	0.000	–	0.445	0.000	–
f_{+0}	0.075	0.000	0.187	0.027	0.000	0.237	0.000	0.000	0.250
ϕ_{+++}	0	π	π	0	π	π	0	π	π
ϕ_{--}	0	π	0	0	π	0	0	π	0
ϕ_{+-}	0	0	–	0	0	–	0	0	–
ϕ_{+0}	0	0	π	0	0	π	0	0	π
ϕ_{0-}	0	0	0	0	0	0	0	0	0

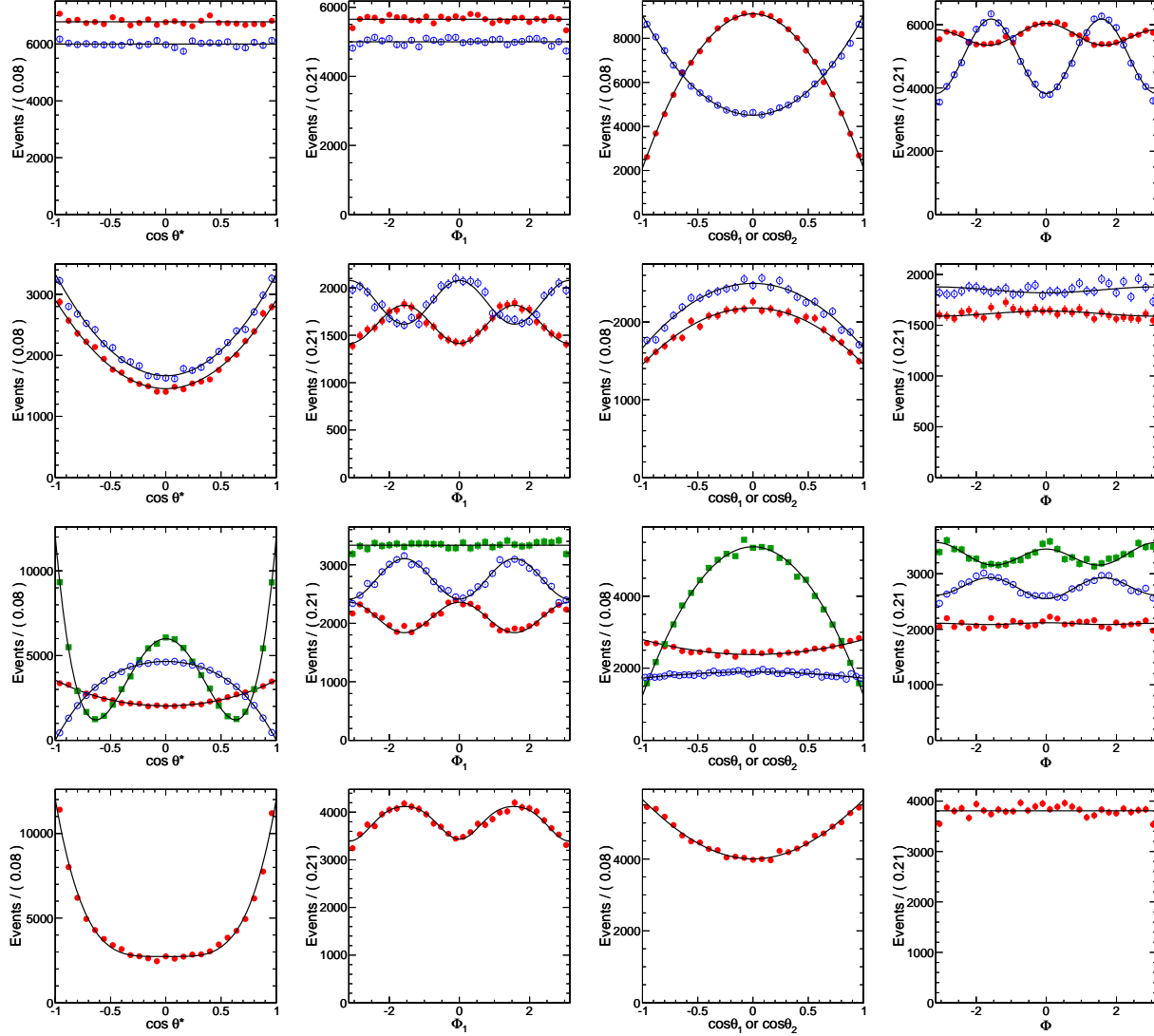


Figure 3: Distribution of the $\cos \theta^*$ (left), Φ_1 (second from the left), $\cos \theta_1$ and $\cos \theta_2$ (second from the right), and Φ (right) generated for $m_X = 250$ GeV (no detector effects considered here) and projections of the ideal angular distributions given (smooth lines). The four sets of plots from top to bottom show the models discussed in Table 1 for spin-zero 0^+ and 0^- (top), spin-one 1^+ and 1^- (second row from top), spin-two 2_m^+ , 2_L^+ , and 2^- (third row from top), and the bottom row shows distributions in $q\bar{q} \rightarrow ZZ$ background generated with Madgraph (points with error bars) and empirical shape (smooth lines). The J^+ distributions are shown with solid red points and J^- distributions are shown with open blue points, while the 2_m^+ and 2_L^+ are shown with red circles and green squares, respectively.

3 Simulation, Reconstruction, and Selection

A dedicated simulation program has been used to generate signal events [24] in the 7 signal scenarios given in Table 1. Pythia [25] is used for hadronization and further interface to the CMS software (CMSSW) framework. For both the fully leptonic and semileptonic final states of the $X \rightarrow ZZ$ resonance, we use fast simulation of the CMS detector performed in the CMSSW_3.4.2 or compatible releases. Specific issues of reconstruction and background studies are given below for each decay channel separately. The CMSSW_3.5.6 or compatible releases are used for reconstruction.

3.1 Reconstruction of $X \rightarrow ZZ \rightarrow 4l$

We fully reconstruct the $X \rightarrow ZZ \rightarrow 4l^\pm$ event candidates. The calculation of the helicity and production angles described in Section 1 has been introduced in the Higgs analysis package [26, 27, 28].

Signal and background data samples are generated using Monte Carlo simulation. For the background processes, we consider the main contributions from (in the order of importance):

- $ZZ^{(*)} \rightarrow 4l$.
- $Zb\bar{b} \rightarrow 2l b\bar{b}$
- $t\bar{t}$

In Table 5, the MC expected cross-sections for relevant processes are given [29]. As mentioned previously, when estimating the yields for comparison between various signal processes, we use as a baseline the case of the SM Higgs. For the case of $E_{pp} = 7$ TeV, we use the dominant background samples $q\bar{q} \rightarrow ZZ$ generated with MadGraph [30] of approximately 1M events in each channel. We also use the generator GG2ZZ [31] for modeling $gg \rightarrow ZZ$ process. While the absolute normalization of the gluon fusion contribution is still uncertain in the generator, we use the calculated fraction of 15% [31] of the gg contribution for studies.

Table 5: Monte Carlo with the estimated cross-sections for background processes. Here Z stands for Z, Z^*, γ^* ; l stands for e, u, τ .

Process	MC	σ_{NLO} BR
$t\bar{t} \rightarrow 2Wb\bar{b}$	NNLL	165 ± 10 pb
$Zb\bar{b} \rightarrow 2l b\bar{b}$	MCFM LO, $m_{ll} > 20$ GeV	67.3 ± 18.8 pb
$q\bar{q} \rightarrow ZZ \rightarrow 4l$	MCFM NLO, $m_{ll} > 40$ GeV	5.9 pb ± 0.2 pb

For the signal Monte Carlo samples for the process $X \rightarrow ZZ \rightarrow 4l^\pm$, we consider the seven scenarios discussed above. In all cases, approximately 100k events of each signal process are simulated with fast simulation considering the detector in the ideal scenario. All signal samples are generated with a mass of the ZZ resonance at $m_{ZZ} = 140, 250, 500$, and 1000 GeV.

The selection requirements for the ZZ resonances follow the strategy laid out in [26]. There, the selection strategy is described in much further detail. Here, we outline only the main points of the overall selection strategy.

The CMS High Level Trigger (HLT) is foreseen to allow for thresholds well below 20 GeV/ c . A global "OR" is taken between different HLT sequences (trigger-paths) to maximize selection efficiency. The trigger-paths under consideration are: single muon isolated, single muon (no isolation), double muon (no isolation), single electron isolated, single electron (relaxed isolation), double electron isolated, and double electron (relaxed isolation). For signal processes, we expect a trigger efficiency for m_{ZZ} above the ZZ threshold which is above 98%. For all background processes, we first ask for 4 leptons at the generator level. In the $t\bar{t}$ and $Zb\bar{b}$ background channels, we also require the generator-level leptons have $p_T > 4$ GeV and $|\eta| < 2.7$. Trigger selection allows for a drastic reduction of event rate while preserving a high reconstruction efficiency for $X \rightarrow ZZ$. As mentioned above, the *reducible* backgrounds dominate after HLT selection. The following strategy to further reduce backgrounds relies on the discriminating observables, isolation, and impact parameter.

The four leptons from an $X \rightarrow ZZ$ resonance should appear from the the primary vertex and appear isolated. In contrast, at least 2 leptons coming from $t\bar{t}$ and $Zb\bar{b}$ backgrounds will appear inside b -jets. The four leptons from signal are also expected to come from a common primary vertex whereas at least one lepton pair should come

from a displaced vertex in the reducible background processes. Thus, the impact parameter for signal events are compatible with zero while the background impact parameter is much larger due to the long b -quark lifetime. By making requirements on the impact parameter of leptons with respect to the primary vertex, further reduction of $t\bar{t}$ and $Zb\bar{b}$ backgrounds can be achieved. Therefore, by using isolation and impact parameter cuts, we are able to further reduce backgrounds present after HLT selection. Ref. [26] provides further details on the isolation and impact parameter cuts.

We make further kinematic cuts based on the p_T of the four leptons, two-lepton invariant masses, and four-lepton invariant mass. For the transverse momentum of the four leptons, p_T^l , we set a minimal threshold of $p_{Tmin}^e > 7$ GeV and $p_{Tmin}^\mu > 5$ GeV. For the invariant mass cuts, we select signal event candidates with loose enough selection on resonance masses to include sidebands for later fitting. For the lepton pair invariant mass, the selection window is $60 < m_{ll} < 105$ GeV for an X resonance mass above the ZZ threshold. For an X mass below the threshold, we relax the lepton pair invariant mass for the Z^* candidate to $10 < m_{ll} < 105$ GeV. The ZZ invariant mass m_{ZZ} window is set for each X resonance mass hypothesis and analysis is repeated for each hypothesis.

Some of the early studies of the angular and mass observables resolutions were performed with the 2-series releases and have not been repeated. However, these studies indicate that resolution is excellent and will not affect angular parameterization. These studies with the 14 TeV MC samples are summarized in Table 6 for several mass points. As an example of the signal and background composition, Fig. 4 shows simulated signal and background for a 250 GeV resonance (RS1 model with $c = 0.1$) with 2/fb of data at LHC energy of 14 TeV.

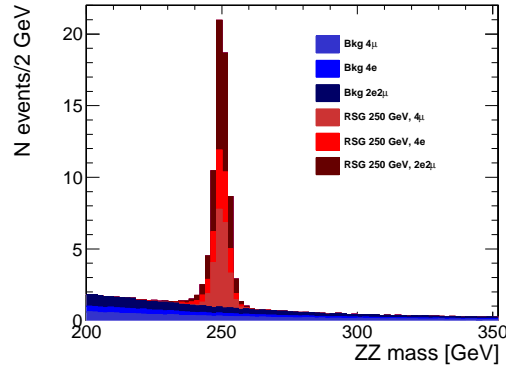


Figure 4: Simulated signal and background for a 250 GeV resonance in the $X \rightarrow ZZ \rightarrow 4l$ channel.

Each event candidate is characterized by a set of six observables $\{m_{ZZ}, \cos\theta^*, \Phi_1, \cos\theta_1, \cos\theta_2, \Phi\}$. In Table 6 we show the effect of the full analysis selection on the Higgs-like resonance. In particular, resolution in the six observables and the selection efficiency are quoted. The Table gives the signal efficiency of the analysis at various mass points.

Table 6: Resolution in the six observables $\{m_{ZZ}, \cos\theta^*, \Phi_1, \cos\theta_1, \cos\theta_2, \Phi\}$ and the selection efficiency of the SM Higgs-like $H \rightarrow ZZ \rightarrow 4l$ resonance decay. Resolution is quoted (in GeV for mass, radians for azimuthal angle, and dimensionless for cos) as the rms of the distributions of the reconstructed value minus the generated value. Reconstruction was done using CMSSW_2.2.11 with the 14 TeV LHC energy MC samples.

Mass	Decay	σ_m	$\sigma_{\cos\theta^*}$	σ_{Φ_1}	$\sigma_{\cos\theta_1}$	$\sigma_{\cos\theta_2}$	σ_Φ	Mass Window	Efficiency
250	4μ	2.6	0.010	0.007	0.018	0.018	0.007	210-280	52.4%
	$4e$	4.0	0.013	0.008	0.022	0.022	0.008	210-280	40.0%
	$2\mu 2e$	3.2	0.013	0.007	0.018	0.020	0.007	210-280	48.6%
500	4μ	7.5	0.010	0.002	0.017	0.017	0.002	300-700	59.2%
	$4e$	5.2	0.011	0.002	0.014	0.014	0.002	300-700	47.7%
	$2\mu 2e$	6.5	0.011	0.002	0.015	0.016	0.002	300-700	42.0%
1000	4μ	24.4	0.011	0.003	0.021	0.021	0.003	900-1050	61.6%
	$4e$	10.0	0.008	0.002	0.014	0.014	0.002	900-1050	54.6%
	$2\mu 2e$	19.1	0.010	0.003	0.016	0.019	0.003	900-1050	45.1%

3.2 Reconstruction of $X \rightarrow ZZ \rightarrow 2l2j$

The study of the decay channel with two leptons and two jets in the reconstructed final state has been carried out in CMSSW_3.6.2. The signal used for the analysis with two leptons (either electrons or muons) and two jets in the final state was generated according to the description in Section 3. The SM backgrounds considered are listed in Table 7. The integrated luminosities listed in the same table refer to the Summer10 production samples with the exception of the di-boson samples are from the Spring10 production samples. All background processes were generated using Pythia6.

Table 7: Monte Carlo datasets used for estimating the SM background to the $X \rightarrow ZZ \rightarrow 2l2j$ final state.

Process	cuts	x-sect [pb]	N events	Int. Lumi [fb^{-1}]
$Z \rightarrow ee + jets$	$m_{ll} > 20 \text{ GeV}$	1666 (NNLO)	2515660	1.51
$Z \rightarrow \mu\mu + jets$	$m_{ll} > 20 \text{ GeV}$	1666 (NNLO)	2548980	1.53
$Z \rightarrow \tau\tau + jets$	$m_{ll} > 20 \text{ GeV}$	1666 (NNLO)	1369452	.822
$ZZ \rightarrow any$		4.3 (LO)	145383	33.81
$WW \rightarrow any$		28 (LO)	122920	4.39
$WZ \rightarrow any$		10.5 (LO)	118125	11.25
$t\bar{t} \rightarrow any$		157.5 (NLO)	603225	3.83
QCD jets ($\hat{p}_T > 170 \text{ GeV}/c$)		28030 (LO)	3171950	0.12

The analysis of the channel $X \rightarrow ZZ \rightarrow 2l2j$ is performed using the Physics Analysis Toolkit (PAT) [32]. Input objects to PAT are GSF electrons, Global Muons, and jets reconstructed with the `anti-kT` algorithm. The radius parameter of the `anti-kT` algorithm was set to $R = 0.5$. A “cleaning” procedure was applied in order to ensure that the same particle was not double counted as two different physics objects.

The electron candidates were required to satisfy the following conditions to ensure well-reconstructed electrons:

- transverse impact parameter with respect to the primary vertex $D_0 < 2 \text{ mm}$;
- combined relative isolation parameter $R = \frac{ECAL_{ISO} + HCAL_{ISO} + TRK_{ISO}}{p_T} < 0.15$;
- RobustLoose Electron ID selection.

Global muons were required to satisfy the following conditions in order to be identified:

- normalized χ^2 of the Tracker track < 10.0 ;
- number of hits of the Tracker track ≥ 11 ;
- $D_0 < 2 \text{ mm}$;
- $R < 0.15$.

Both electrons and muons were required to be in the pseudorapidity range $|\eta| < 2.5$ and have a transverse momentum $p_T > 10 \text{ GeV}/c$. The invariant mass of the $Z \rightarrow l^+l^-$ boson was required to be $70 < m_{ll} < 110 \text{ GeV}$.

The energy of the jets was corrected for their flavor content (L5 JECs) before applying a JetID based on the set of requirements called `CRAFT08Tight`. This Jet ID requires

The $Z \rightarrow jj$ candidates were built out of the possible combinations of the jets passing the JetID and with an invariant mass $70 < m_{jj} < 120 \text{ GeV}$. The following kinematic selection was required on jets

- $p_{T,j_1} > 40 \text{ GeV}/c$;
- $p_{T,j_2} > 30 \text{ GeV}/c$;
- $|\eta| < 2.5$,

where j_1 and j_2 refer to the jets ordered in decreasing transverse momentum.

From all the possible combinations of $Z \rightarrow 2l$ and $Z \rightarrow 2j$, resonance candidates were built requiring the invariant mass m_{ZZ} to be in a specified mass range above 190 GeV . When more than one candidate is present in an event

after all the final selection requirements, the best candidate was chosen with the di-jet and the di-lepton invariant masses closest to the mean Z mass value [33]. This is equivalent to picking one combination with the smallest χ^2 :

$$\chi^2 = \frac{(m_{ll} - m_Z)^2}{\sigma_{ll}} + \frac{(m_{jj} - m_Z)^2}{\sigma_{jj}} \quad (4)$$

However, with the present selection the values of σ_{ll} and σ_{jj} do not affect the selection because the χ^2 decouples into two independent χ^2 expressions for the $Z \rightarrow 2l$ and $Z \rightarrow 2j$ candidates independently.

The issue of multiple candidates per event is more important in the analysis of the final state with jets due to higher combinatorics with jet candidates. In Fig. 5 this is illustrated with the Number of events with certain number of event candidates in analysis of a resonance with the mass of 500 GeV. The typical number of candidates per event is 1.34. The choice of an event candidate with the best mass Z invariant mass maximizes the probability of the right candidate choice when more than one is present. Since the Z invariant mass is not used further in analysis after tight selection requirement, there is no bias in analysis. However, if the Z invariant mass is further used, more care should be taken to describe its artificial peaking towards the mean, or different choices could be investigated.

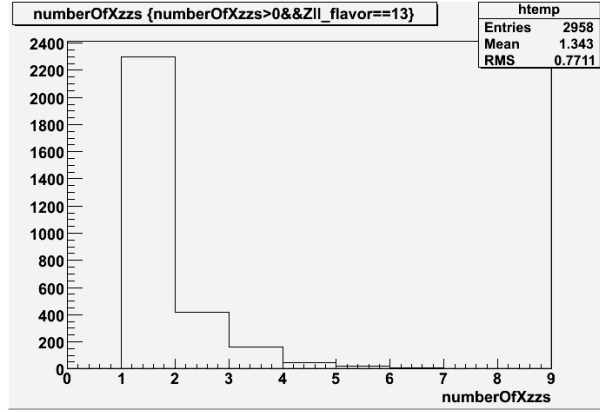


Figure 5: Number of events with certain number of event candidates in analysis of a resonance with the mass of 500 GeV.

In Table 8 we show the effect of the full analysis selection on the Higgs-like resonance. In particular, resolution in the six observables and the selection efficiency are quoted. The Table gives the signal efficiency of the analysis at various mass points.

Table 8: Resolution in the six observables $\{m_{ZZ}, \cos \theta^*, \Phi_1, \cos \theta_1, \cos \theta_2, \Phi\}$ and the selection efficiency of the SM Higgs-like $H \rightarrow ZZ \rightarrow 2l2j$ resonance decay. Resolution is quoted as the RMS of the distributions of the reconstructed value minus the generated value. Reconstruction was done using CMSSW_3.6.2. Since resolution is dominated by the jet reconstruction, the same resolution parameters are shown for the electron and muon channels.

Mass	Decay	σ_m	$\sigma_{\cos \theta^*}$	σ_{Φ_1}	$\sigma_{\cos \theta_1}$	$\sigma_{\cos \theta_2}$	σ_{Φ}	Mass Window	Efficiency
250 GeV	$2\mu 2j$	16.28	0.067	0.077	0.047	0.13	0.42	200-300	21.9%
	$2e 2j$	16.28	0.067	0.077	0.047	0.13	0.42	200-300	21.0%
500 GeV	$2\mu 2j$	26.26	0.047	0.032	0.024	0.12	0.48	300-700	38.1%
	$2e 2j$	26.26	0.047	0.032	0.024	0.12	0.48	300-700	44.5%
1000 GeV	$2\mu 2j$	38.35	0.043	0.027	0.023	0.14	0.53	800-1200	15.3%
	$2e 2j$	38.35	0.043	0.027	0.023	0.14	0.53	800-1200	16.7%

3.3 Expected reconstructed yields

In Tables 9 and 10 we present the number of signal and background events expected with 1/fb of data with an LHC energy of 7 TeV. When the expected number of background events is significantly smaller than one, we conservatively enhance expectation to one background event, to be conservative and to technically allow the method of toy MC technique for studies. As it is evident from Table 10, this is mostly relevant for the largest mass point $m_X = 1000$ GeV. In the pessimistic scenario, zero signal is assumed to contribute. In the realistic scenario, assume

20 signal events in the $4l$ sample and the corresponding number of events in the $2l2j$ sample (roughly an order of magnitude larger). This corresponds to the yield in the RS graviton (G_{RS}) model with $c = 0.1$ at $m_X = 500$ GeV. The rationale for this choice is that this yield roughly corresponds to the Tevatron [22] limit across the wide range of masses, as indicated in Fig. 2.

We should note that the for G_{RS} cross-section in Table 10 the K-factor of 1.5 is included. The K-factor correction mainly comes from the $gg \rightarrow G$ vertex. This vertex-correction effect is a long distance effect compared to the hard scattering. So it is relatively insensitive to the exact resonance from the gg fusion. Therefore, the value from the Higgs decay could be used since both are gg fusion dominant. This factor is larger than the $q\bar{q} \rightarrow Z'$ value since the gg vertex has larger color concentration. We take the factor 1.5 as the typical ratio between the (N)NLO and LO Higgs predictions [23]. The SM Higgs (H_{SM}) calculation is performed at NNLO [23]. Cross-sections for Higgs production in the gluon fusion channel are computed using the tool HggTotal (NNLO). Small contribution due to VBF are computed using the tool VV2H. The branching ratios of the SM Higgs are computed using the tool HDECAY v.3.4. The HggTotal (NNLO) prediction is checked against HIGLU (at NLO) and is typically 50% higher, which is equivalent to using a K-factor with the NLO prediction.

We should also note that the typical reconstruction efficiency in the $H \rightarrow 4l$ analysis is about 50%, see Table 6 for example and Refs. [26, 27, 28]. Therefore, further assumptions about the yield quoted in Table 10 are based on 50% reconstruction efficiency in the $H \rightarrow 4l$ channels, while the 3-series efficiency numbers are still being finalized.

Table 9: Cross-sections (σ , in fb) and the number of expected events (N) for various processes which are background to the $X \rightarrow ZZ$ process with different lepton and jet final states. The number of events corresponds to 1/fb of data with LHC energy of 7 TeV.

Background Channels				
$\sigma(q\bar{q} \rightarrow ZZ \rightarrow 4l); l = e, \mu$	18.3 fb			
$\sigma(gg \rightarrow ZZ \rightarrow 4l); l = e, \mu, \tau$	2.5 fb			
	120-160	210-280 GeV	300-700 GeV	900-1050 GeV
$N(q\bar{q} \rightarrow ZZ \rightarrow 4e)$	~ 0.75	0.62	0.36	~ 0
$N(q\bar{q} \rightarrow ZZ \rightarrow 2e2\mu)$	~ 1.50	2.6	1.5	~ 0
$N(q\bar{q} \rightarrow ZZ \rightarrow 4\mu)$	~ 0.75	1.4	0.79	~ 0
$N(gg \rightarrow ZZ \rightarrow 4e)$	~ 0	0.023	0.012	~ 0
$N(gg \rightarrow ZZ \rightarrow 2e2\mu)$	~ 0	0.17	0.080	~ 0
$N(gg \rightarrow ZZ \rightarrow 4\mu)$	~ 0	0.051	0.024	~ 0
	–	200-300 GeV	300-700 GeV	800-1200 GeV
$N(Zjj \rightarrow 2\mu 2j)$		1079	449	6.6
$N(Zjj \rightarrow 2e 2j)$		1376	560	5.2
$N(ZZ \rightarrow 2\mu 2j)$		14.3	6.8	.03
$N(ZZ \rightarrow 2e 2j)$		12.3	5.9	.06
$N(ZW \rightarrow 2\mu 2j)$		32.3	28.0	.68
$N(ZW \rightarrow 2e 2j)$		29.4	20.7	1.4
$N(t\bar{t}) (2\mu 2j)$		87.2	14.1	.26
$N(t\bar{t}) (2e 2j)$		70.2	15.9	~ 0
$N(WW) (2\mu 2j)$.09	~ 0	~ 0
$N(WW) (2e 2j)$.18	~ 0	~ 0
$N(QCD) (2\mu 2j)$		~ 0	~ 0	~ 0
$N(QCD) (2e 2j)$		~ 0	~ 0	~ 0
$N(\text{total}) (2\mu 2j)$		1491	592	6.9
$N(\text{total}) (2e 2j)$		1179	480	6.1

Table 10: Cross-sections (σ , in fb), branching fractions (\mathcal{B}), and the number of expected events (N) for various $X \rightarrow ZZ$ processes expected with 1/fb of data with LHC energy of 7 TeV. For G_{RS} , the K-factor of 1.5 is included. SM Higgs (H_{SM}) calculation is performed at NNLO, only gluon fusion production is considered; NLO VBF production contribution ~ 5 -10%. Lepton final states assume $l = e, \mu$, unless otherwise noted, and hadronic jets are denoted with j . Three RS graviton (G_{RS}) models are considered with three plausible values of scale c .

Signal Channels				
	140 GeV	250 GeV	500 GeV	1 TeV
$\sigma(H_{SM} \rightarrow ZZ^{(*)})$	9.26×10^2	1.14×10^3	2.40×10^2	-
$\sigma(G_{RS} \rightarrow ZZ)$ at $c = 0.01$	-	1.94×10^3	6.83×10^1	1.41
$\sigma(G_{RS} \rightarrow ZZ)$ at $c = 0.05$	-	4.83×10^4	1.69×10^3	3.53×10^1
$\sigma(G_{RS} \rightarrow ZZ)$ at $c = 0.1$	-	1.94×10^5	6.76×10^3	1.41×10^2
$\mathcal{B}(H_{SM} \rightarrow ZZ^{(*)})$	0.068	0.295	0.260	-
$\mathcal{B}(G_{RS} \rightarrow ZZ)$	-	0.052	0.049	0.046
$\mathcal{B}(ZZ \rightarrow 4l)$	$\sim 0.067 \times 0.067 \simeq 4.48 \times 10^{-3}$			
$\mathcal{B}(ZZ \rightarrow 2l2j)$	$\sim 2 \times 0.067 \times 0.699 \simeq 8.96 \times 10^{-2}$			
$N(H_{SM} \rightarrow ZZ^{(*)} \rightarrow 4\mu)$	0.52	0.64	0.13	-
$N(H_{SM} \rightarrow ZZ^{(*)} \rightarrow 4e)$	0.52	0.64	0.13	-
$N(H_{SM} \rightarrow ZZ^{(*)} \rightarrow 2\mu 2e)$	1.04	1.28	0.27	-
$N(H_{SM} \rightarrow ZZ \rightarrow 2\mu 2j)$	-	22.4	38.9	-
$N(H_{SM} \rightarrow ZZ \rightarrow 2e 2j)$	-	21.5	45.5	-
$N(G_{RS} \rightarrow ZZ \rightarrow 4\mu)$ at $c = 0.01$		1.7	0.06	0.0013
$N(G_{RS} \rightarrow ZZ \rightarrow 4e)$		1.7	0.06	0.0013
$N(G_{RS} \rightarrow ZZ \rightarrow 2\mu 2e)$		3.4	0.12	0.0025
$N(G_{RS} \rightarrow ZZ \rightarrow 4\mu)$ at $c = 0.05$		42.9	1.4	0.028
$N(G_{RS} \rightarrow ZZ \rightarrow 4e)$		42.9	1.4	0.028
$N(G_{RS} \rightarrow ZZ \rightarrow 2\mu 2e)$		85.8	2.8	0.055
$N(G_{RS} \rightarrow ZZ \rightarrow 4\mu)$ at $c = 0.1$		162	5.3	0.11
$N(G_{RS} \rightarrow ZZ \rightarrow 4e)$		162	5.3	0.11
$N(G_{RS} \rightarrow ZZ \rightarrow 2\mu 2e)$		324	10.6	0.22

4 Analysis Techniques

After reconstruction and selection, we have a sample of N signal event candidates which are characterized by a set of several observables (which can be easily extended with other kinematic quantities) $\vec{x}_i = \{m_1, m_2, m_{ZZ}, \cos \theta^*, \Phi_1 \cos \theta_1, \cos \theta_2, \Phi\}_i$. These include the five production and helicity angles, the resonance invariant mass m_{ZZ} , and m_1 and m_2 which are the invariant masses of the two Z candidates. While we keep the option of including $m_{1,2}$ open, we typically apply relatively tight selection requirements, but otherwise exclude the two masses m_1 and m_2 from further analysis (fit) for several reasons. First of all, the dominant backgrounds have real $Z \rightarrow l^+ l^-$ candidates and therefore its invariant mass provides no separation power, while there is a danger of introducing correlations between the $m_{1,2}$ and m_{ZZ} variables, which are tricky to deal with in the fit. In the case of a dijet decay $Z \rightarrow jj$, we prefer to use the dijet invariant mass to choose the best event candidate, and therefore its distribution is biased in the background. On the other hand, the $Z^* \rightarrow l^+ l^-$ invariant mass m_2 , in the case of a below- ZZ -threshold resonance production, is an important quantity for parameterization and is kept in the fit.

We use an unbinned, extended maximum-likelihood (ML) fit [34] to extract simultaneously the signal and background yields, the background parameterization, and characterization of the signal angular distributions. The likelihood function is written as:

$$\mathcal{L} = \exp(-n_{\text{sig}} - n_{\text{bkg}}) \prod_i^N \left(n_{\text{sig}} \mathcal{P}_{\text{sig}}(\vec{x}_i; \vec{\zeta}; \vec{\xi}) + n_{\text{bkg}} \mathcal{P}_{\text{bkg}}(\vec{x}_i; \vec{\xi}) \right), \quad (5)$$

where n_j is the unconstrained number of events for each event type j (signal or background), $\mathcal{P}_j(\vec{x}_i; \vec{\zeta}; \vec{\xi})$ is the probability density function, again for signal and background. Each event candidate i is characterized by a set of several observables \vec{x}_i . The signal polarization parameters are denoted by $\vec{\zeta}$, and the remaining parameters by $\vec{\xi}$.

We perform a joint fit to the data for the sub-channels: three sub-channels in the $4l$ final state 4μ , $4e$, and $2e2\mu$; two sub-channels in the $2l2j$ final state $2\mu2j$ and $2e2j$; and all five sub-channels when all ZZ final states are combined. In the joint fit, the likelihood function \mathcal{L} is written as a product of several independent likelihood functions, one for each of up to five modes. For signal we use the sum of all contributing yields as the fitting parameter, and constrain the ratio of the yields to the expected efficiency ratio. The backgrounds yields of the sub-channels are also related according to expectation, which is the same efficiency ratio as for signal for the dominant background in the $4l$ channels or $2l2j$ channels.

4.1 Parameterization of the probability density functions

For signal, the probability density function $\mathcal{P}_{\text{sig}}(\vec{x}_i; \vec{\zeta}; \vec{\xi})$ is taken to be a joint 5D function for the production and helicity angles, as discussed in Appendix A, and a 1D function for the X resonance mass. However, for analysis of a resonance below ZZ threshold, the joint 6D function of five angles and dimuon mass of $Z^* \rightarrow l^+ l^-$ is taken instead of the 5D function, see Appendix B. For background, the probability density function is parameterized in a similar manner, though some simplification is possible if background contribution is small. More specifically, we also parameterize the production and helicity angles with a 5D correlated function when the background is substantial, as for example in analysis of a resonance at 250 GeV. However, at higher masses, a much smaller background is expected and the probability density function is taken as the product of uncorrelated functions for each observable. The assumption of small correlations is further tested with the toy MC experiments. As long as the toy MC experiment results are unbiased, small correlations are acceptable.

4.2 Parameterization of the signal angular distributions: lepton channels

It was found with detailed MC simulation that resolution effects in the angles, see Table 6, introduce negligible effects in the parameterization and fit performance and they are therefore ignored. The resolution effects are somewhat larger in the channels with jets, see Table 8, but we still find it acceptable to ignore them in parameterization in favor of great reduction in complexity of the fit. However, if the latter resolution effects are incorporated in the angular parameterization with convolution in the probability density function, only modest improvements on hypothesis separation is expected. In either case, the present results can be considered as conservative.

The helicity probability density function for signal is the ideal distribution discussed in Appendix A multiplied by an empirically-determined acceptance function $\mathcal{G}(\cos \theta^*, \Phi_1, \cos \theta_1, \cos \theta_2, \Phi)$ which is a parameterization of the relative reconstruction efficiency as a function of helicity angles. We approximate the acceptance function by $\mathcal{G} = \mathcal{G}^{(1)}(\cos \theta^*) \times \mathcal{G}^{(2)}(\Phi_1) \times \mathcal{G}^{(3)}(\cos \theta_1) \times \mathcal{G}^{(4)}(\cos \theta_2) \times \mathcal{G}^{(5)}(\Phi)$, neglecting all correlations between different

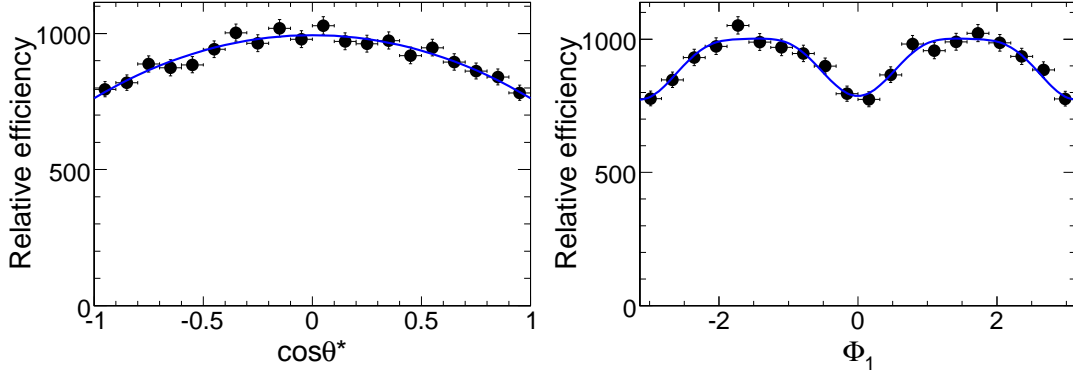


Figure 6: Parameterization of acceptance effects for the $\cos \theta^*$ (left) and Φ_1 (right) for the case of a 250 GeV resonance production. These plots show only relative efficiency between different points with arbitrary y -axis units.

angles. While a better and formally more correct parameterization is possible and is desired to achieve high precision, the present approach was found acceptable in toy MC studies, also see Ref. [10] for more discussion.

The rationale for the acceptance function parameterization is the following. The three helicity angles between the final state particles and their parent resonances are related to their momenta, which introduces kinematic correlations, whereas the detector geometry correlations are negligible. Therefore, the three helicity angles have little correlations and little effect in their acceptance (acceptance function is essentially flat). One exception is the helicity angle of the dijet decay $Z \rightarrow jj$, where requirement on the jet energy may introduce a rather strong kinematic effect, which is taken into account in $\mathcal{G}^{(4)}(\cos \theta_2)$. On the other hand, the two production angles are strongly correlated with the geometry of the detector since they are defined with respect to the collision axis. Particles lost along the beampipe introduce strong effect in both $\cos \theta^*$ and Φ_1 angles, as discussed in Ref. [10]. An example of parameterization of acceptance effects for the $\cos \theta^*$ and Φ_1 for the case of a 250 GeV resonance $X \rightarrow ZZ \rightarrow 4\mu$ is shown in Fig. 6.

An example of the angles for the Standard Model Higgs Monte Carlo are shown in Fig. 7. One can compare these to the distributions in Fig. 3, the main difference now is the presence of detector acceptance effects. In each case, the parameterization shown is a projection of the 5D function which includes the acceptance effects. It is important to note that all angular distributions are truly 5D, and 1D projections cannot reflect that (though for a spin-zero particle they are truly 3D since production angles are not correlated). This also means that performing a 5D angular analysis is essential, while a 1D angular analysis will not have sufficient information to differentiate hypotheses. All seven X resonance hypotheses are generated and parameterized in a similar manner.

4.3 Parameterization of background angular distributions: lepton channels

We show the example of angular distributions for background in Fig. 8. These background distributions have been generated with MadGraph for $q\bar{q}$ (85%) and with GG2ZZ for gg (15%) and are shown for the mass window around 250 GeV. We take special care to parameterize correlations in the angular distribution of the background in the following way. First, we use a large number of generated events without detector effects. The most general angular distribution can in principle be parameterized as an infinite sum of different spin contributions (from zero and up to a large number) with each contribution parameterized with Eq. (6) from Appendix A with the appropriate spin index. However, we make certain simplifications to avoid infinite sum as discussed below.

Second, we use a large number of generated events (from the same sample as above) after detector reconstruction. This sample has acceptance effects introduced. We therefore parameterize acceptance in the same way as we parameterize it for signal with an effective function $\mathcal{G}_{\text{bkg}} = \mathcal{G}^{\text{bkg}(1)}(\cos \theta^*) \times \mathcal{G}^{\text{bkg}(2)}(\Phi_1) \times \mathcal{G}^{\text{bkg}(3)}(\cos \theta_1) \times \mathcal{G}^{\text{bkg}(4)}(\cos \theta_2) \times \mathcal{G}^{\text{bkg}(5)}(\Phi)$. Thus, we achieve a similar level of sophistication in parameterization of angular distributions in signal and background. Moreover, we note that our approach also allows certain parameterization of background to be left free in the fit, and therefore perform angular analysis of ZZ “background,” which is an interesting EWK signal on its own. Just as an example, one could fit for relative fraction of $q\bar{q}$ and gg production mechanisms, or go further and perform partial wave analysis in certain intervals of invariant mass.

In the angular parameterization of the ideal background distributions (without detector effects), we first parameterize the helicity angular distributions $(\cos \theta_1, \cos \theta_2, \Phi)$ with one set of effective parameters f_{ij} and ϕ_{ij} using

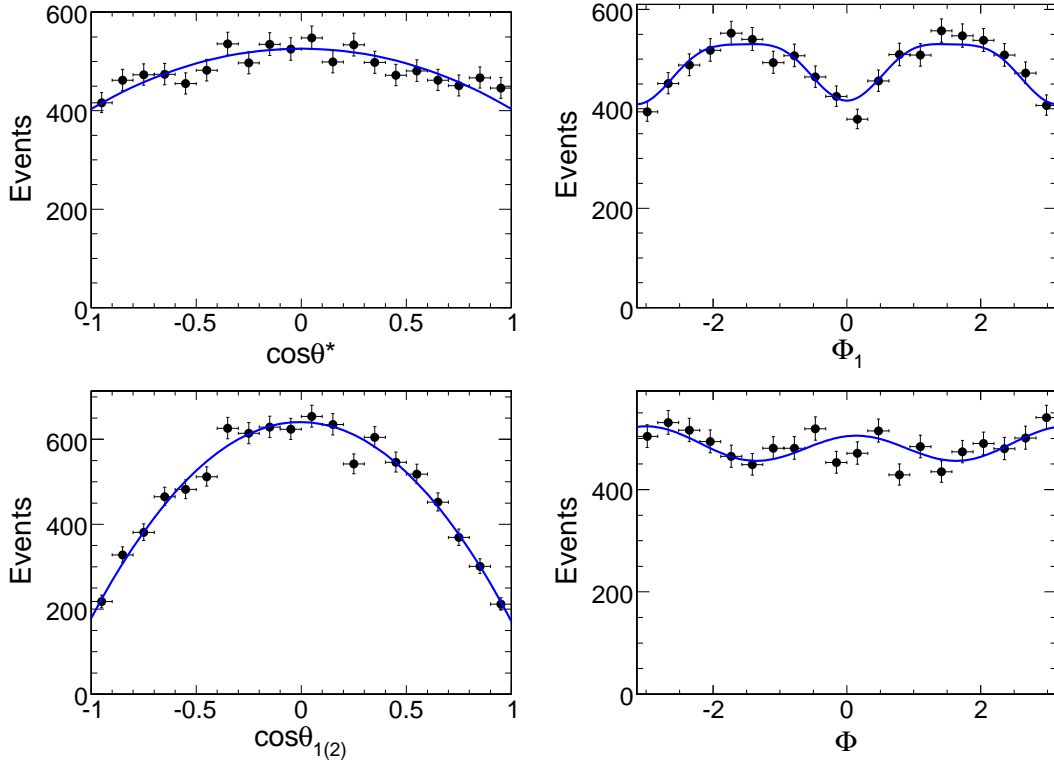


Figure 7: Examples of the angular distributions $\cos\theta^*$ (top left), Φ_1 (top right), $\cos\theta_{1,2}$ (bottom left), Φ (bottom right) for the fast simulation of SM scalar Higgs decay $H \rightarrow ZZ \rightarrow 4\mu$ with 250 GeV mass.

Eq. (6) after integrating out $\cos\theta^*$ and Φ_1 (Ψ). This provides formally correct (up to statistical precision in the method) 3D correlated parameterization. Then we extend this parameterization to an effective 5D correlated parameterization by introducing these parameters into the full Eq. (6), where instead of $F_{ij}(\theta^*)$ functions we take polynomial functions of $\cos\theta^*$ with even power up to 8, therefore ignoring contributions of high spin in the series. The resulting angular distributions, also after introducing the acceptance effects, match well the data, as shown in Fig. 8.

In Fig. 9 we show Examples of the ideal (prior to detector effects) angular distributions for the simulation of electro-weak non-resonant processes $q\bar{q} \rightarrow ZZ \rightarrow 4\mu$ and $gg \rightarrow ZZ \rightarrow 4\mu$. The values of the helicity amplitude parameters are quoted in Table 11. As it can be seen, there is relatively large fraction of the longitudinal contribution in the $gg \rightarrow ZZ$ process (f_{00}), while there is relatively large spin-projection-two transverse contribution in the $q\bar{q} \rightarrow ZZ$ process (f_{+-}). These may become distinguishing features of the two mechanisms and may help to separate production mechanism in the di-boson production on LHC.

Table 11: Fractions of the various helicity amplitudes in the $q\bar{q} \rightarrow ZZ$ and $gg \rightarrow ZZ$ electro-weak non-resonant processes as measured with a generated sample in the mass range 210-280 GeV. The typical statistical errors are 0.009 or less.

parameter	$q\bar{q} \rightarrow ZZ$	$gg \rightarrow ZZ$
f_{00}	0.025	0.398
f_{++}	0.206	0.430
f_{--}	0.005	0.012
f_{+0}	0.007	0.047
f_{0-}	0.147	0.007
f_{+-}	0.228	0.026

4.4 Parameterization of angular distributions: channels with jets

As mentioned above, despite the finite resolution of some variables in this channel, resolution effects are assumed to be negligible. This assumption is corroborated to a large extent by the quality of fits show in Fig. 10, which

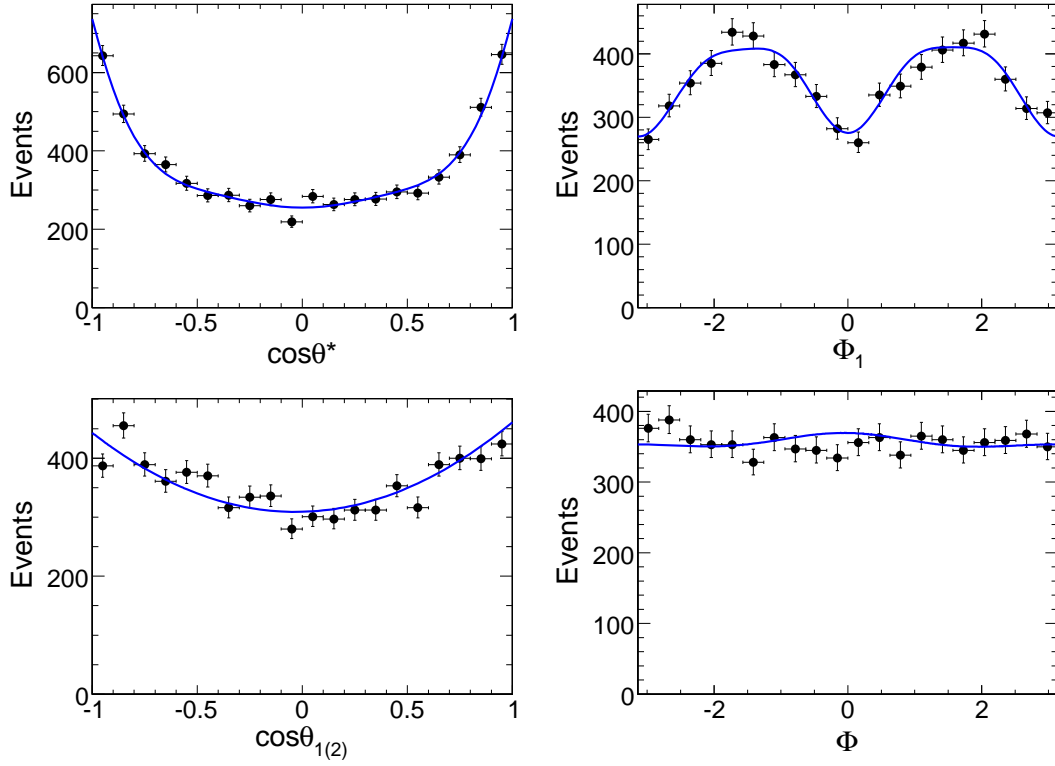


Figure 8: Examples of the angular distributions $\cos\theta^*$ (top left), Φ_1 (top right), $\cos\theta_{1,2}$ (bottom left), Φ (bottom right) for the simulation of $q\bar{q}$ and $gg \rightarrow ZZ \rightarrow 4\mu$ in the mass range 210-280 GeV.

reflects the angular distributions well. Therefore, more detailed treatment of the angular resolution is not essential with the expected signal statistics. However, acceptance has considerable effects on several variables. Comparison of Fig. 10 with ideal angular distributions of a 0^+ signal, Fig. 3, demonstrates the acceptance effect. These detector effects are assumed to arise mostly from p_T cuts on the jet objects. The acceptance effect was accounted for in the angular distributions by multiplying the ideal distributions by an effective function $\mathcal{G}_{\text{bkg}} = \mathcal{G}^{\text{bkg}(1)}(\cos\theta^*) \times \mathcal{G}^{\text{bkg}(2)}(\Phi_1) \times \mathcal{G}^{\text{bkg}(3)}(\cos\theta_1) \times \mathcal{G}^{\text{bkg}(4)}(\cos\theta_2) \times \mathcal{G}^{\text{bkg}(5)}(\Phi)$, analogous to what was done for the lepton only channel.

The parameterization of background was found by fitting a product of polynomials and finite Fourier series to the data. In this way, all correlations are assumed to be negligible and the shapes of the different variables are assumed to be known. While we fully take into account correlations of the angular distributions in the signal due to spin correlations, such correlations are less important in background due to non-resonant nature of the main background Z +jets. Nonetheless, studies of the angular correlations in background are possible in principle, but will require much higher statistics in the simulated samples. An example of background parameterization is shown in Fig. 11.

4.5 Parameterization of the invariant mass distributions

A relativistic spin- J Breit-Wigner (BW) amplitude parameterization is used for the resonance masses. Even though the width of the resonance may become another model-dependent method to separate different hypothesis, we intentionally decouple this feature from the studies of angular distributions and use the same width of the resonance for all hypothesis. We take this width to be the one expected for a SM Higgs up to 500 GeV, while we take the width to be negligibly small at 1 TeV since Higgs prediction does not make sense any more at such a large mass. The Breit-Wigner parameterization is convoluted with asymmetric resolution function, which is found to be best described by the Crystal Ball function. See Fig. 12 for illustration of this approach for a Higgs mass distribution at 250 GeV. However, in some cases we simplify this parameterization for speed of the toy MC studies, which we find to be an acceptable approach as long as the function matches the distributions. Mass parameterizations used in toy MC studies at 250 GeV are shown in Fig. 13.

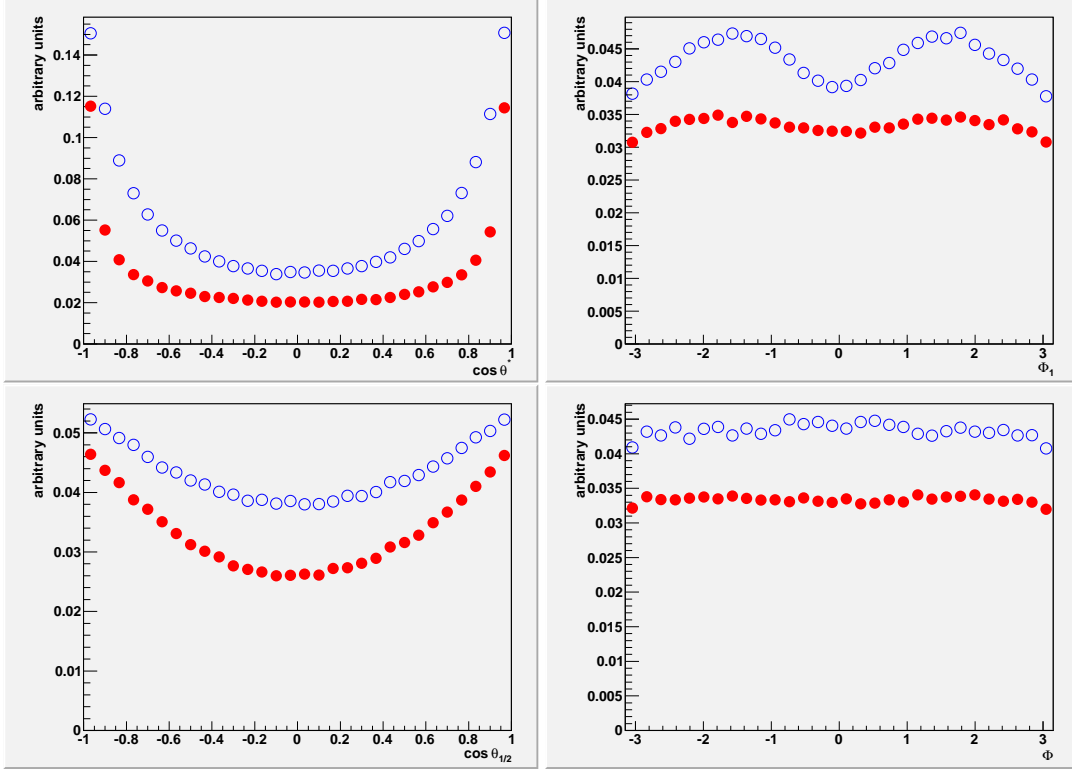


Figure 9: Examples of the ideal (prior to detector effects) angular distributions $\cos \theta^*$ (top left), Φ_1 (top right), $\cos \theta_{1,2}$ (bottom left), Φ (bottom right) for the simulation of electro-weak non-resonant processes $q\bar{q} \rightarrow ZZ \rightarrow 4\mu$ (open blue points) and $gg \rightarrow ZZ \rightarrow 4\mu$ (solid red points) in the mass range 210-280 GeV.

4.6 Parameterization below the ZZ threshold

The fit implementation for analysis of a resonance below the ZZ mass threshold is very similar to above the threshold, but there are several special features which require special care. First of all, there is one additional observable in the fit, the $Z^* \rightarrow l^+l^-$ invariant mass m_2 . The expected distribution of m_2 for different types of signal (such as 0^+ and 0^-) is discussed in Appendix B. However, there is an additional effect which changes the shape of the reconstructed distribution. In Fig. 14 we show the ratio of the reconstructed and generated distributions of m_2 for the Higgs sample, using full detector simulation. Due to kinematic selection on the lepton momentum, there is lower efficiency to reconstruct events with lower values of m_2 . We choose to discard events with extremely low $m_2 < 10$ GeV and parameterize the effect with a mass acceptance function $\mathcal{G}_m(m_2)$, similarly to the acceptance function for the angles. The resulting probability density function is a product of the mass acceptance function and the ideal angular distribution. However, for initial feasibility study we ignore this effect, as well as the effect of the finite width of the on-shell Z boson. The used mass distributions are shown in Fig. 15 for two types of signal (0^+ and 0^-) and for background. These were generated with the MC simulation program discussed in Ref. [10]. The overall probability density function is a correlated 6D mass-angular parameterization discussed in Appendix B and multiplied by the acceptance functions in both mass and angles. This 6D parameterization is also multiplied by a 1D parameterization of the m_{ZZ} observable. For the feasibility studies in this note, we concentrated only on the spin-0 resonances below ZZ threshold. In this case only four variables are correlated: three helicity angles and m_2 . We combine these four variables with the ZZ invariant mass in this feasibility analysis.

4.7 Validation and study techniques

To test the signal parameterization and the overall fit performance, we generate a large number of MC experiments, each one representing a statistically independent modeling of the fit to the data. The signal events are taken randomly from the generated signal MC samples and background events are taken randomly from the background MC samples. The number of signal and background events is taken according to model discussed earlier, e.g. 20 or 0 signal and certain number of background events. We find the results of the MC experiments to be in good agreement with expectations and the error estimates to be correct. In Fig. 16, we show examples of the n_i^{fitted} and $(n_i^{\text{fitted}} - n_i^{\text{generated}})/\sigma(n_i)$ distributions, where n_i denotes the signal yield. The mean and width of the pull

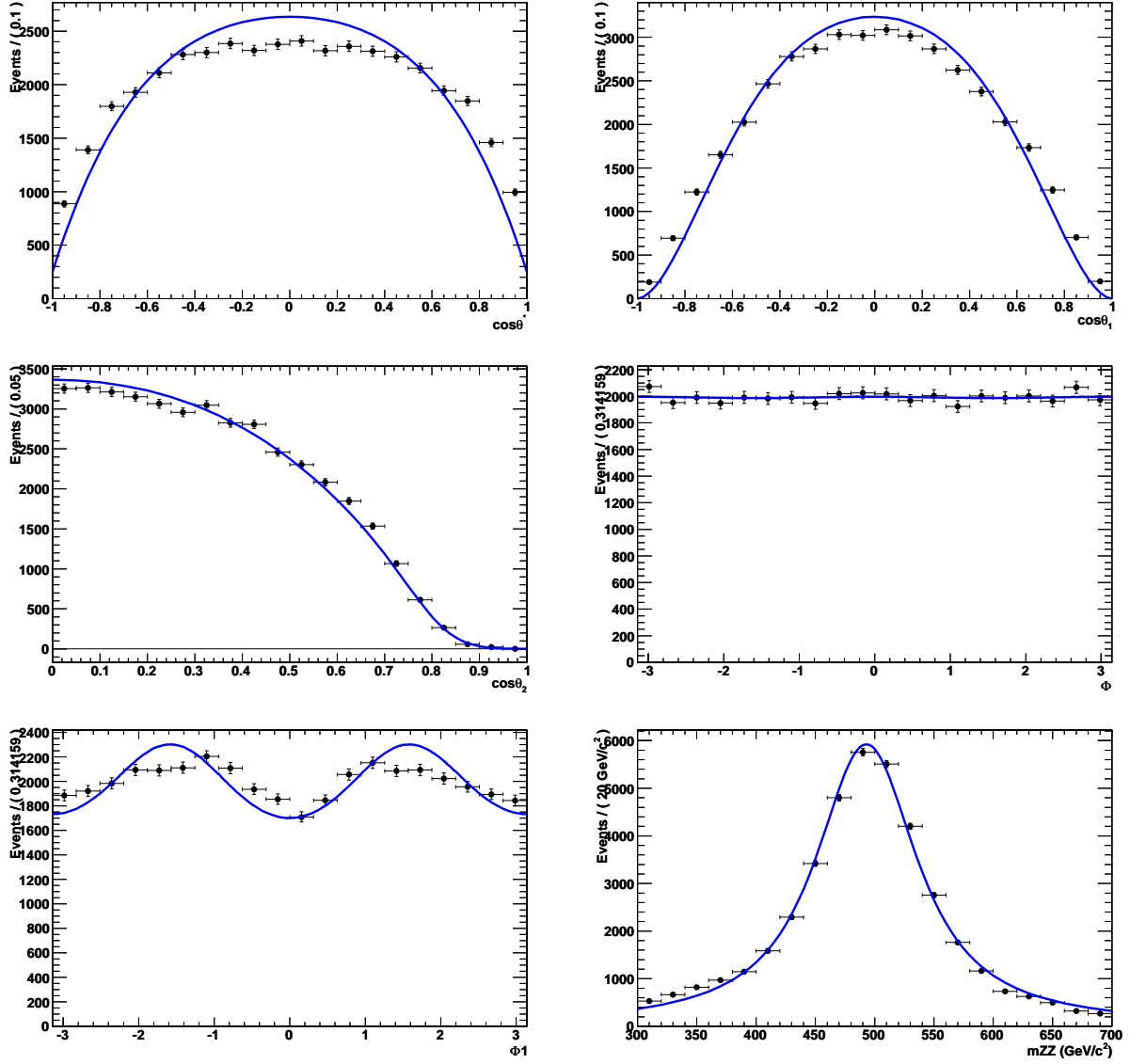


Figure 10: Example of the angular distributions of $\cos \theta^*$ (top left), $\cos \theta_1$ (top right), $\cos \theta_2$ (middle left), Φ (middle right), Φ_1 (bottom left), and the di-boson invariant mass (bottom right) for the fast simulation of SM scalar Higgs decay $H \rightarrow ZZ \rightarrow 2l2j$ with 500 GeV mass.

distribution are within about 10% of the expected values of zero and one, which results in small uncertainty in the fit result.

The significance of the signal yields is defined as the square root of the change in $2 \ln \mathcal{L}$ when the yield is constrained to zero in the likelihood \mathcal{L} . An example of expected signal significance with 20 signal and 6 background events is shown in the left plot of Fig. 17. The significance corresponds to the Gaussian probability for pure background to fluctuate to the observed yield. The desired property of the significance estimator is illustrated in the right plot of Fig. 17 where only background was generated with 51 events. The probability for observing results with $> 1, 2, 3\sigma$ follows Gaussian statistics (observed fraction of 15.0, 2.11, 0.14% with the expectation of 15.9, 2.27, 0.14%).

We can also test how well different signal models of an observed resonance X could be separated. We calculate the likelihood \mathcal{L} in Eq. (5) independently for the hypotheses of angular distributions denoted with parameters $\vec{\zeta}_1$ and $\vec{\zeta}_2$. The two resulting likelihood values \mathcal{L}_1 and \mathcal{L}_2 can be used to construct the quantity $2 \ln(\mathcal{L}_1/\mathcal{L}_2)$. The discussion of the statistical interpretation of $2 \ln(\mathcal{L}_1/\mathcal{L}_2)$ was given recently in Ref. [35]. The distribution of $2 \ln(\mathcal{L}_1/\mathcal{L}_2)$ is expected to peak at positive values for events generated according to model one (on average $\mathcal{L}_1 > \mathcal{L}_2$) and at negative values for events generated according to model two (on average $\mathcal{L}_2 > \mathcal{L}_1$).

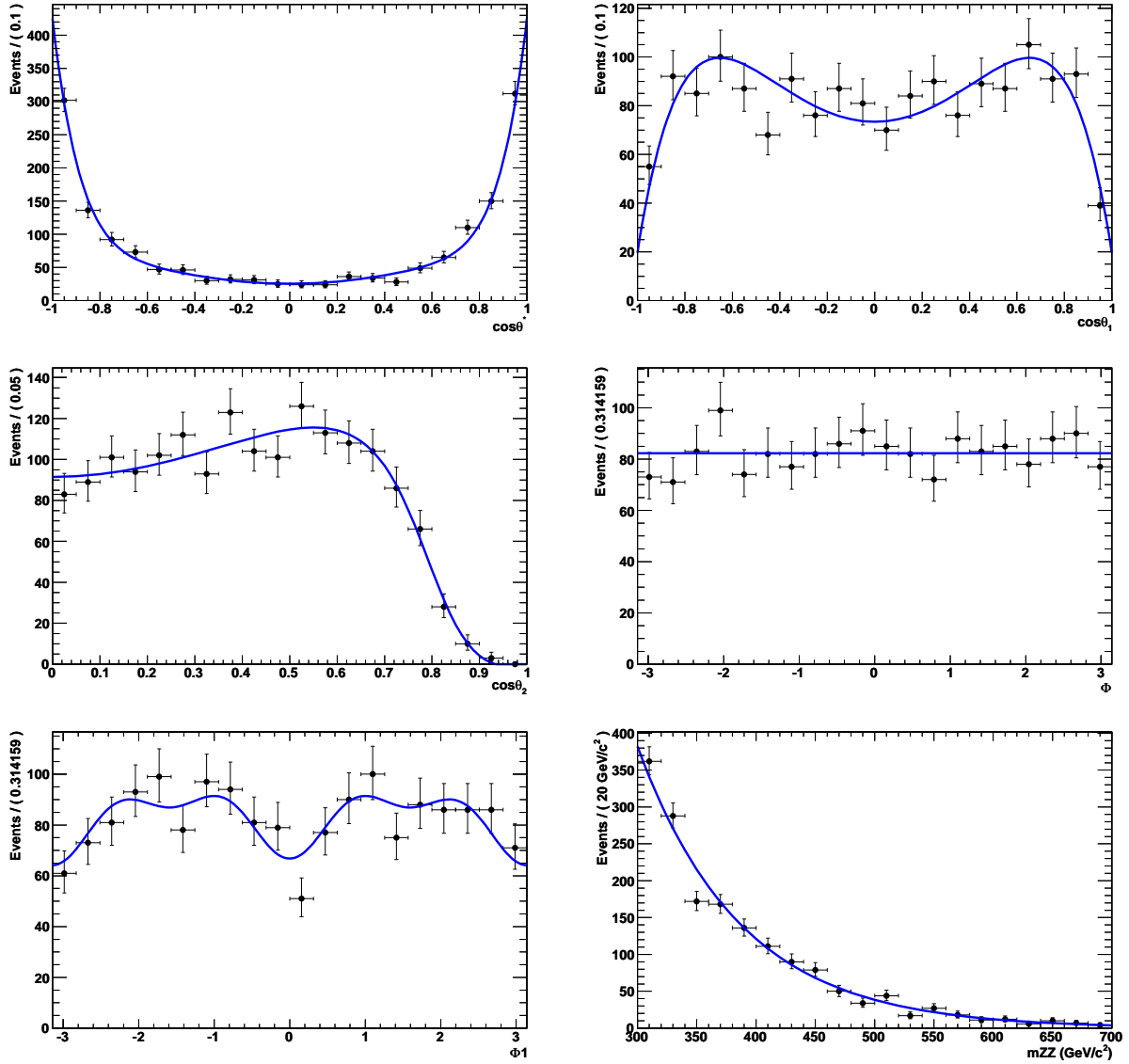


Figure 11: Example of the angular distributions of $\cos \theta^*$ (top left), $\cos \theta_1$ (top right), $\cos \theta_2$ (middle left), Φ (middle right), Φ_1 (bottom left), and the di-boson invariant mass (bottom right) for the fast simulation of SM $Z \rightarrow l\bar{l} + Jets$ events in the mass range of 300 GeV-500 GeV.

As an example, in Fig. 18, we show such a distribution for the comparison of 0^+ and 0^- , as well as 0^+ and 2_m^+ , hypotheses for a resonance of 250 GeV. From Fig. 18, we extract the quantity S in the following way. We find the point beyond which the right-side tail of the left histogram (fraction f) and the left-side tail of the right histogram have equal areas. These areas correspond to the one-sided Gaussian probability outside of the $S/2$ σ range. If the two histograms in Fig. 18 were perfectly Gaussian distributed with unit width, then S corresponds to the separation between the peaks of the two distributions. The above procedure is repeated for all combinations of seven hypotheses listed in Table 1 and for different masses and results are presented in the next Section. The value of S should correspond to the tail of the Gaussian probability distribution and satisfies $\text{TMath}::\text{Prob}(S \times S/4, 1)/2 = f$.

All of the above tests could be performed if signal is found. However, if no signal is found, one can set a limit on the number of signal events of a certain type, and as a result, on the production cross-section. We calculate the 95% CL upper limit as the number of events above which only 5% of the likelihood distribution lies. We exclude non-physics negative even counts from consideration. As an example, in Fig. 19 we show distribution of the 95% CL upper limit on the number of signal SM Higgs events at 250 GeV. The average limit improves from 6.5 to 5.8 events after including angular information.

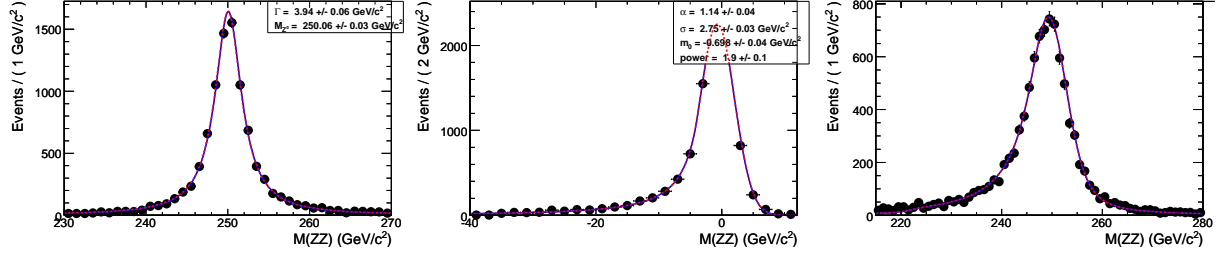


Figure 12: The invariant mass distributions for a Higgs resonance $H \rightarrow ZZ \rightarrow \mu^+\mu^-e^+e^-$ at 250 GeV. Left: ideal BW distribution at generator level, no detector effects present. Middle: difference between reconstructed and generated invariant masses parameterized with Crystal Ball function. Right: reconstructed invariant mass parameterized with BW function convoluted with Crystal Ball function, both extracted from the other two plots.

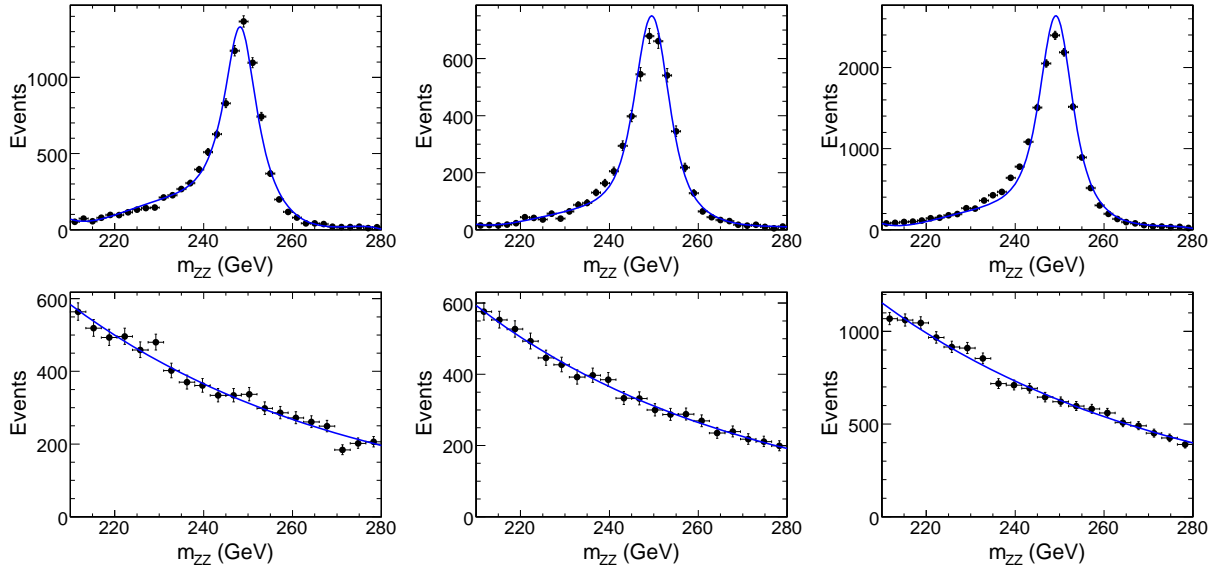


Figure 13: Top: example of the resonance ZZ mass for the Standard Model Higgs at 250 GeV. Bottom: example of the ZZ resonance mass for background. The three sub-channels are shown from left to right: 4μ , $4e$, and $2e2\mu$.

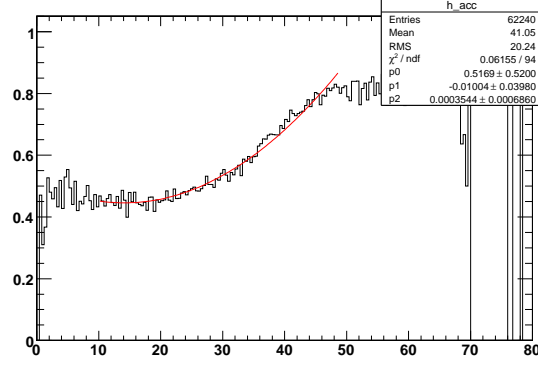


Figure 14: The ratio of the reconstructed (with detector effects) and generated distributions of the $Z^* \rightarrow l^+l^-$ invariant mass m_2 for the Higgs sample.

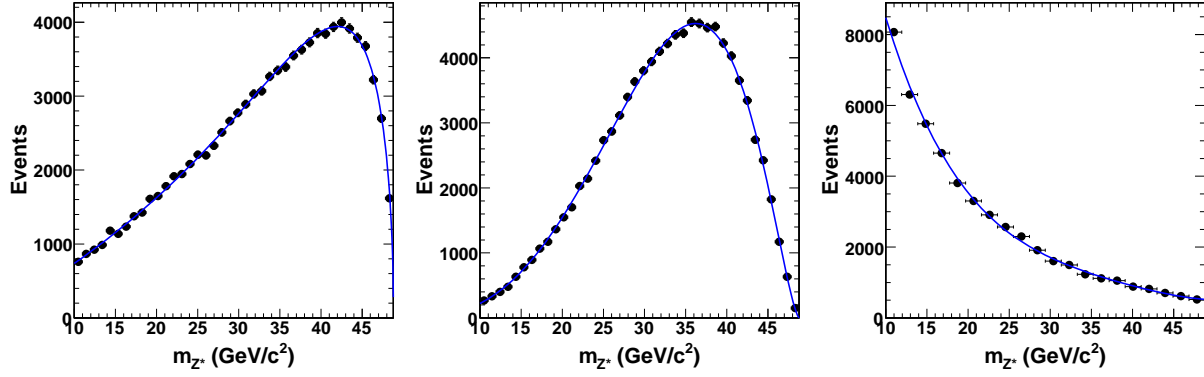


Figure 15: Projection on the $Z^* \rightarrow l^+l^-$ invariant mass m_2 for three samples: signal 0^+ (left), signal 0^- (middle), and background (right).

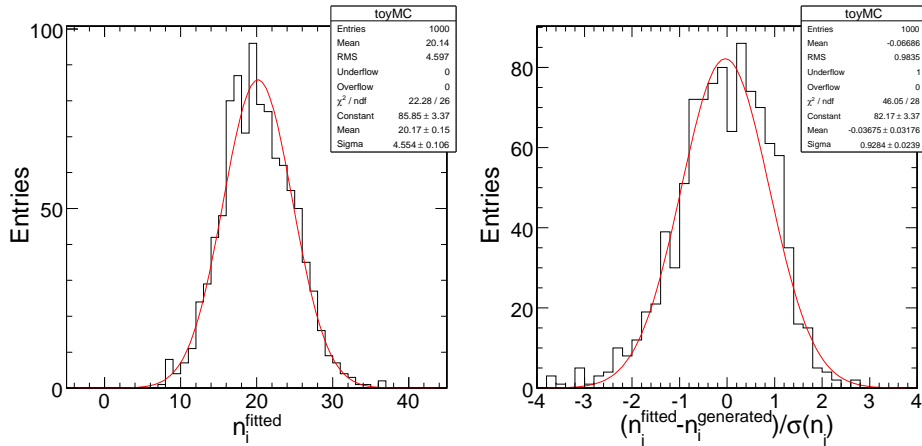


Figure 16: Distributions of n_i^{fitted} (left) and $(n_i^{\text{fitted}} - n_i^{\text{generated}}) / \sigma(n_i)$ (right) for a large number of generated MC experiments, where a Gaussian fit is superimposed, and n_i denotes n_{sig} . The $n_i^{\text{generated}}$ corresponds to 5, 5, and 10 signal Standard Model Higgs events for the three sub-channels 4μ , $4e$, and $2\mu 2e$ generated with fast simulation. The number of background events was set according to Table 9.

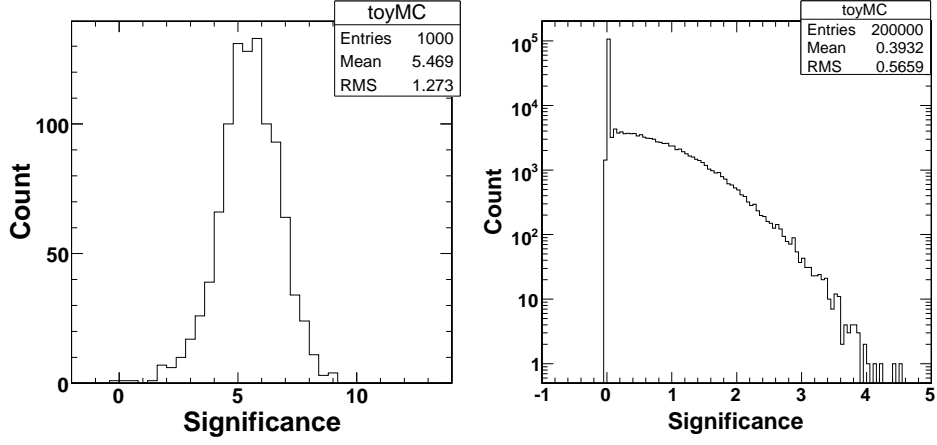


Figure 17: Left: distributions of the signal yield significance in the toy MC experiments with 6 background events and 20 signal Standard Model Higgs events generated with fast simulation. Right: the same distribution, but with 51 background events and no signal.

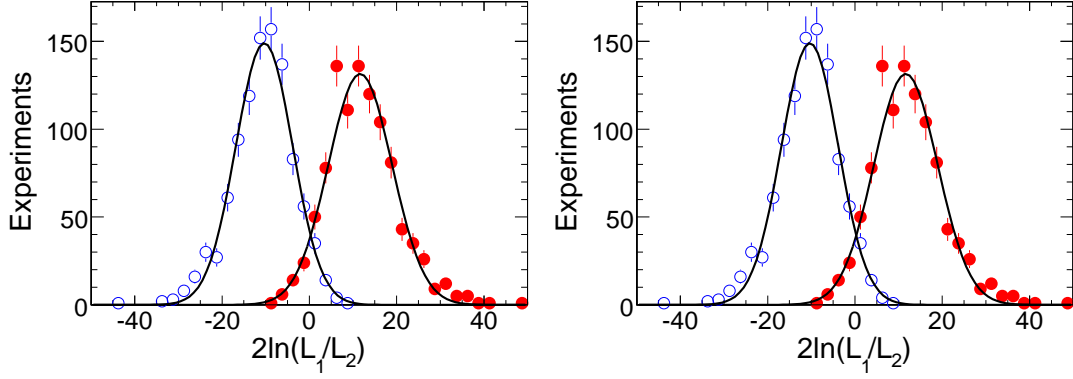


Figure 18: Distribution of $2 \ln(\mathcal{L}_1/\mathcal{L}_2)$ with the likelihood \mathcal{L} evaluated for two models $k = 1, 2$ and shown for 1000 generated experiments with the MC events generated according to model one ($k = 1$, open dots) and model two ($k = 2$, solid dots). Left plot: 0^+ vs. 0^- ; right plot: 0^+ vs. 2_m^+ . Effective signal hypothesis separation power S is 3.3 (left plot) and 2.2 (right plot).

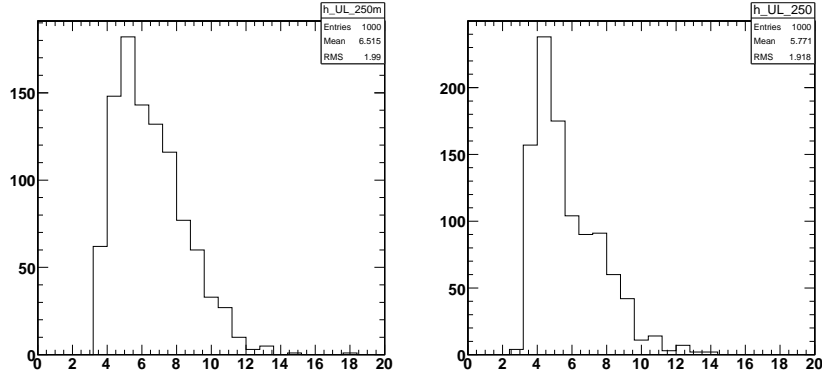


Figure 19: Distribution of the 95% CL upper limit evaluated from the likelihood distribution for 1000 generated experiments of SM Higgs. Left plot: only invariant mass is considered in the fit; right plot: both mass and five angles are included in the fit.

5 Results

The first question that we address in these studies is what kind of upper limit could be set on a resonance at different ZZ invariant mass with 1/fb of data collected at LHC energy of 7 TeV, assuming that no resonance actually exists. Therefore, we perform 1000 toy MC experiments at each mass point of 140, 250, 500, and 1000 GeV. Only background events are embedded in this study, and no signal events are introduced. These results are summarized in Table 12. The distributions of the upper limit values are shown in Figs. 19 and 20, from which the average value is taken as input in Table 12. One can note that the upper limit could be improved by about 15% if the angular information is used in the fit. If Fig. 22 the expected upper limits in the $4l$, $2l2j$, and combined analyses are shown, as well as SM expectation for SM Higgs production. It is important to note that the channels with jets provides comparable sensitivity to the lepton channel already at $m_{ZZ} = 250$ GeV, while it dominates at higher masses due to much larger efficiency in the presence of manageable background in early data.

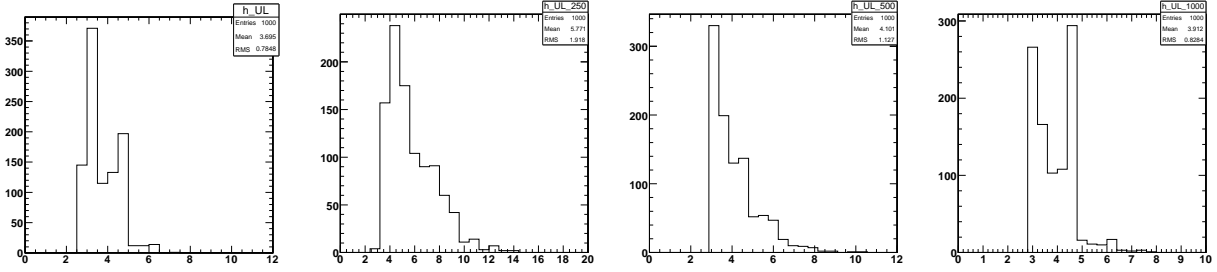


Figure 20: Distribution of the 95% CL upper limit evaluated from the likelihood distribution for 1000 generated experiments of SM Higgs $H \rightarrow 4l$ at 140 GeV (left), 250 GeV (second from the left), 500 GeV (second from the right), and 1000 GeV (right).

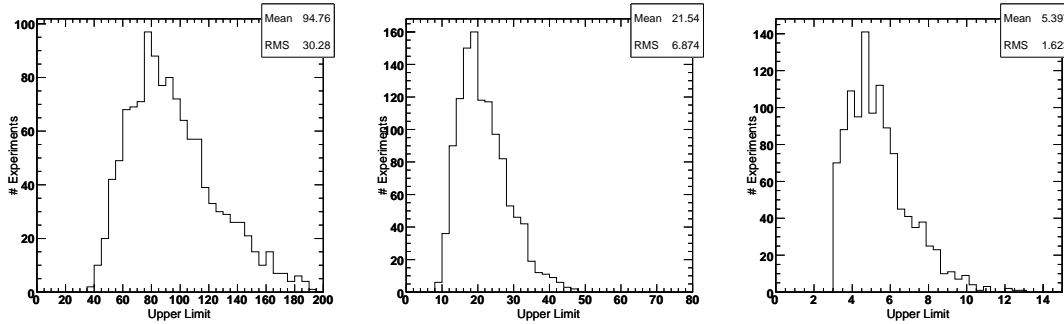


Figure 21: Distribution of the 95% CL upper limit evaluated from the likelihood distribution for 1000 generated experiments of SM Higgs $H \rightarrow 2l2j$ at 250 GeV (left), 500 GeV (middle), and 1000 GeV (right).

Table 12: Upper limits at 95% CL upper limits expected in the analysis of $X \rightarrow ZZ \rightarrow 4l$, and $2l2j$ with the first LHC run (1/fb at 7 TeV). The number of events (N) and production cross-sections (σ , for the process $H_{\text{SM}} \rightarrow ZZ$) are quoted. In the $X \rightarrow ZZ \rightarrow 4l$ channel, 50% reconstruction efficiency is assumed for masses 250 GeV and above, and 30% at 140 GeV.

	140 GeV	250 GeV	500 GeV	1000 GeV
$N(4l)$	3.7	5.8	4.1	3.9
$N(4l)$ (mass only)	5.0	6.5	4.6	4.4
$N(2l2j)$	–	94.8	21.5	5.4
$N(2l2j)$ (mass only)	–	109.6	40.7	6.4
$\sigma(4l)$	2747	2584	1827	1738
$\sigma(2l2j)$	–	4718	556	360
$\sigma(H_{\text{SM}})$	926	1140	240	–

We have also performed a cross-check of the multidimensional likelihood fit with the $X \rightarrow ZZ \rightarrow 2l2j$ channel with four methods, including the nominal fit as well:

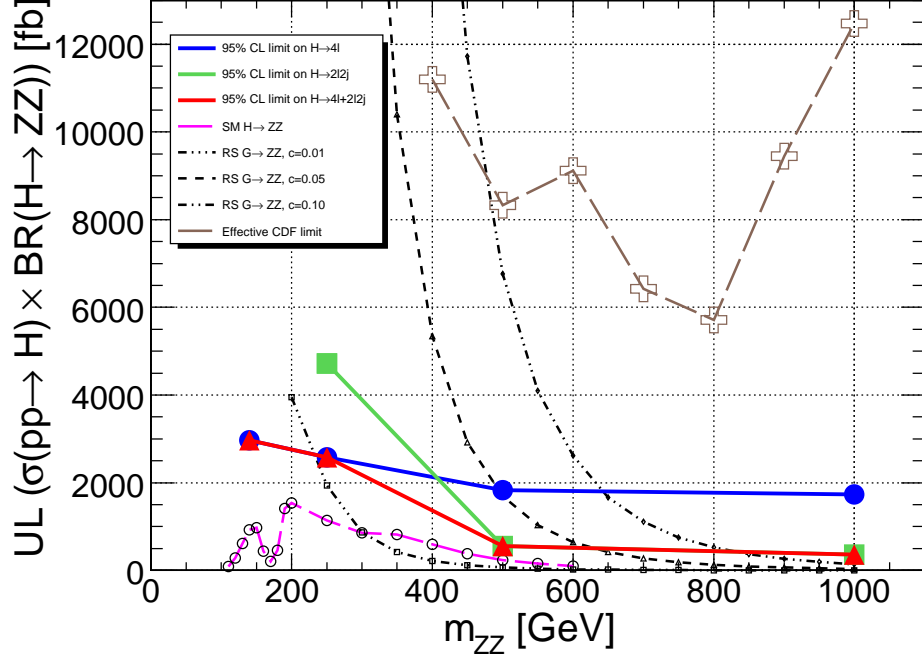


Figure 22: Expected upper limits at 95% C.L. on the cross-section of the SM Higgs production $pp \rightarrow H \rightarrow ZZ$, which also includes branching fraction of the ZZ final state, for the first LHC run (1/fb at 7 TeV). Three expectations for the $4l$ (blue circles), $2l2j$ (green boxes), and combined analyses (red triangles) are shown, as well as SM expectation for SM Higgs production (open circles connected with dashed lines), expectation for RS graviton with three different values of c , and effective limit from Tevatron (CDF 2.9/fb) which is rescaled based on the RS graviton $c=0.1$ expectation at Tevatron and LHC.

- likelihood fit with 6 variables (5 angles and 1 ZZ invariant mass);
- likelihood fit with 1 variable (ZZ invariant mass);
- cut-and-count approach with the ZZ invariant mass background taken from MC;
- cut-and-count approach with the ZZ invariant mass sidebands to estimate background.

The results of these four approaches are compared in Fig. 24 and Table 13. There is statistical improvement as more information and more variables are used in the analysis. We should note that when the five angles are excluded from the analysis (in the last three cases), the analysis is not the most optimal any more as further selection could be applied on the angles. However, the comparison between the three approaches without angles is fair and all three of them use the same input.

Table 13: Expected upper limits at 95% CL in the analysis $H \rightarrow ZZ \rightarrow 2l2j$ using the cut and count approach.

	250	500	1000
σ (w/ errors)	6850	1978	671
σ (w/o errors)	5246	1478	561
σ (likelihood-mass only)	5455	1052	427
σ (likelihood)	4718	556	360

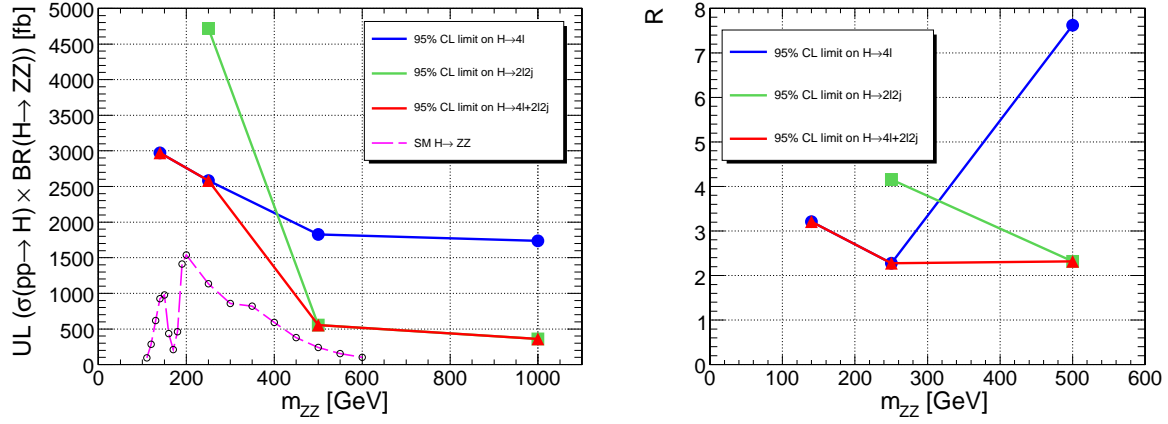


Figure 23: Left plot: same as Fig. 22, but zoomed into the SM Higgs production range. Right plot: ratio of expected upper limits shown on the left plot to the SM Higgs production rate also shown on the left plot.

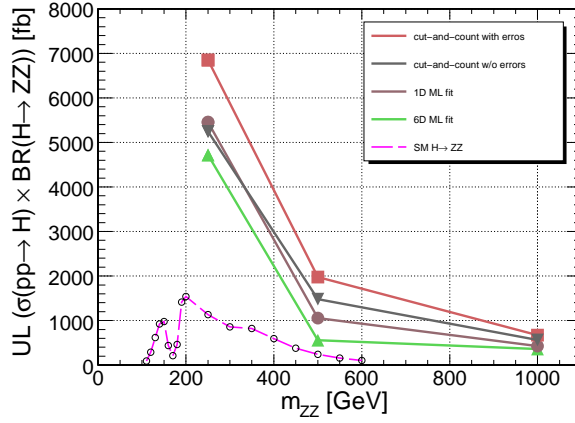


Figure 24: Expected upper limits at 95% C.L. on the cross-section of the SM Higgs production $pp \rightarrow H \rightarrow ZZ$ using the semileptonic final state. Four statistical methods are compared: 6D fit, 1D fit, cut-and-count with known background, cut-and-count with background estimated from sideband.

The next study shows how well one can separate different signal models assuming that a resonance is found with 20 events of $X \rightarrow ZZ \rightarrow 4l$. This is shown in Tables 14–17. Some of the likelihood-ratio distributions are shown in Figs. 18 and 25. Our findings are generally similar to those of Ref. [10], but they are now supported by the full CMS detector simulation. Moreover, we have investigated in more detail the mass point below the ZZ threshold and show the proper treatment of the Z^* mass.

A similar study with the $X \rightarrow ZZ \rightarrow 2l2j$ final state is shown in Table 18 and Fig. 26, where only spin-0 hypothesis are shown for illustration. The number of signal events in this study is scaled according to efficiency and the branching fraction of the $X \rightarrow ZZ \rightarrow 2l2j$ final state with respect to 20 events of $X \rightarrow ZZ \rightarrow 4l$, and is typically between 10 and 20 times large. Therefore, despite higher background, the semileptonic final state provides more statistical power for angular analysis at the higher resonance masses.

Studies of angular analyses of both $X \rightarrow ZZ \rightarrow 2l2j$ and $4l$ final state show that despite various detector effects, including worse angular resolution in the channel with jets, angular information is still retained to large extent and the full angular analysis provides very strong statistical power.

Table 14: Results of the hypothesis separation of the 0^+ and 0^- scenarios for $m_X = 140$ GeV.

0^-	
0^+	3.3

Table 15: Results of the hypothesis separation (S) of the seven scenarios for $m_X = 250$ GeV. with the $X \rightarrow ZZ \rightarrow 4l$.

	0^-	1^+	1^-	2_m^+	2_L^+	2^-
0^+	3.3	1.8	2.0	2.2	1.5	2.7
0^-		2.6	2.4	1.7	3.9	2.2
1^+			1.7	1.7	2.4	2.1
1^-				1.1	2.5	2.4
2_m^+					2.8	2.1
2_L^+						3.3

Table 16: Results of the hypothesis separation (S) of the seven scenarios for $m_X = 500$ GeV. with the $X \rightarrow ZZ \rightarrow 4l$.

	0^-	1^+	1^-	2_m^+	2_L^+	2^-
0^+	4.3	2.6	2.9	3.6	1.3	2.7
0^-		2.7	2.6	1.9	4.6	2.8
1^+			1.9	1.9	3.1	1.9
1^-				1.8	3.2	2.1
2_m^+					4.0	2.7
2_L^+						3.0

Table 17: Results of the hypothesis separation (\mathcal{S}) of the seven scenarios for $m_X = 1$ TeV with the $X \rightarrow ZZ \rightarrow 4l$.

	0^-	1^+	1^-	2_m^+	2_L^+	2^-
0^+	4.7	2.9	2.9	4.1	0.8	2.9
0^-		2.8	2.8	1.9	4.4	2.7
1^+			2.0	2.0	3.0	2.0
1^-				1.9	2.8	2.2
2_m^+					3.9	2.6
2_L^+						2.8

Table 18: Results of the hypothesis separation (\mathcal{S}) with the $X \rightarrow ZZ \rightarrow 2l2j$ at three mass points.

m	0^+ vs 0^-
250 GeV	4.7
500 GeV	>5
1000 GeV	>5

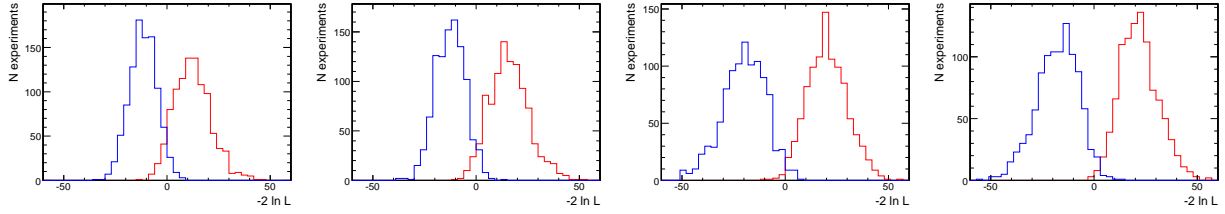


Figure 25: Distribution of $2 \ln(\mathcal{L}_1/\mathcal{L}_2)$ with the likelihood \mathcal{L} evaluated for two models 0^+ and 0^- and shown for 1000 generated experiments with the MC events generated according to model one (0^+) and model two (0^-). Four mass points are considered with the four-lepton final state: 140 GeV (left), 250 GeV (middle left), 500 GeV (middle right), and 1000 GeV (right).

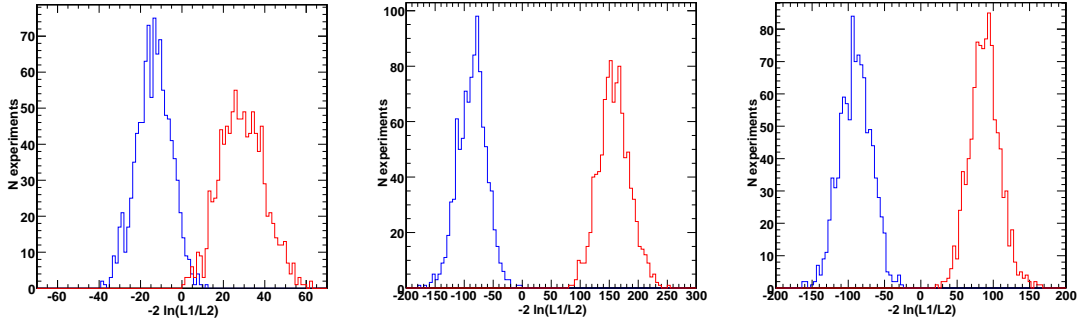


Figure 26: Distribution of $2 \ln(\mathcal{L}_1/\mathcal{L}_2)$ with the likelihood \mathcal{L} evaluated for two models 0^+ and 0^- and shown for 1000 generated experiments with the MC events generated according to model one (0^+) and model two (0^-). Three mass points are considered with the $2l2j$ final state: 250 GeV (left), 500 GeV (middle), and 1000 GeV (right).

6 Analysis of the First ZZ Event

As of the end of 2010 LHC run, only one golden candidate $ZZ \rightarrow 4l$ has been reconstructed on CMS, and it came earlier than expected with the probability for this to happen of less than 10%. This event was collected on Friday September 24, 2010, 02:29:58 CET, in Run 146511, Event 504867308. The kinematics of this event is the following (no systematic errors considered):

- $m_{ZZ} = 201.75$ GeV;
- $m_{\mu\mu 1} = 92.15$ GeV;
- $m_{\mu\mu 2} = 92.24$ GeV;
- $\cos \theta^* = 0.731$;
- $\Phi_1 = -0.460$;
- $\cos \theta_1 = 0.566$;
- $\cos \theta_2 = 0.325$;
- $\Phi = -1.240$.

Since no information on the mass consistency can be obtained with one event, we exclude mass from further consideration and perform a likelihood fit with one event using five angular observables, where angular distributions are fixed to those expected for a particular hypothesis at around 200 GeV. Table 19 summarizes the results of hypothesis testing, where we quote $\chi^2 = 2 \ln(\mathcal{L}_1/\mathcal{L}_2)$. For example for comparison of 0^+ vs. ZZ the $\chi^2 = -0.36$ means that the ZZ hypothesis is slightly more likely than the SM Higgs. However, the confidence level of any exclusion is very small with just one event, therefore we do not go into more detailed hypothesis separation study using the \mathcal{S} significance estimator. We also leave the analysis of the $ZZ \rightarrow 2l2j$ final state with data for future studies because this channel is dominated by the non- ZZ background and therefore requires more detailed treatment and understanding of background. However, once there is sufficient statistics in the $ZZ \rightarrow 4l$ channel and sufficient understanding of background in the $ZZ \rightarrow 2l2j$ channel, full angular analysis of both topologies will be essential.

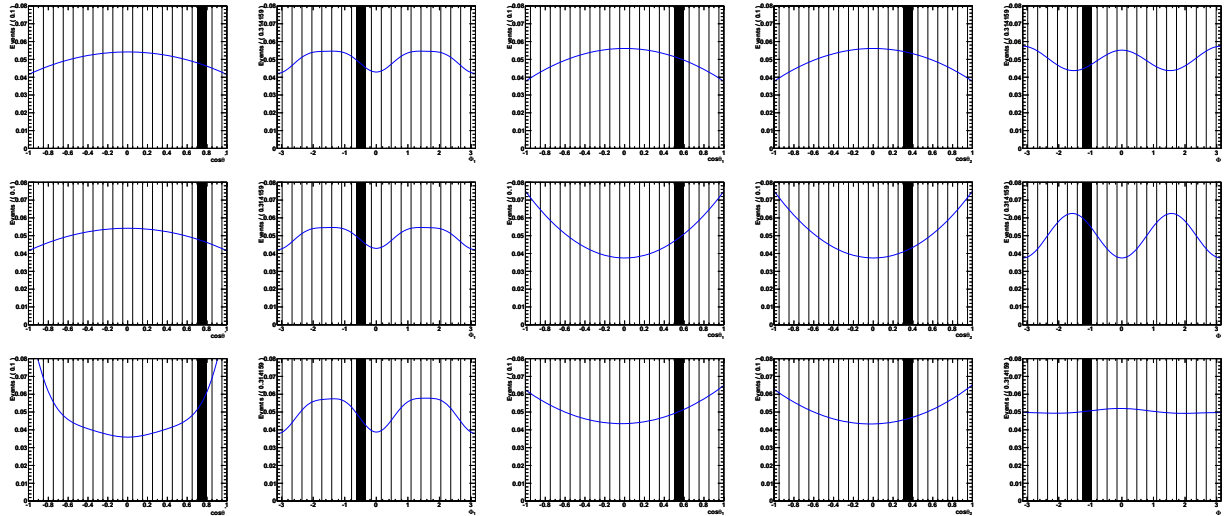


Figure 27: Distribution of the five angular observables for the first $ZZ \rightarrow 4l$ event candidate on CMS (from left to right): $\cos \theta^*$, Φ_1 , $\cos \theta_1$, $\cos \theta_2$, Φ . The thick vertical line shows the measured values and the continuous distributions represent the expectations in three scenarios: SM Higgs 0^+ resonance (top); non-SM Higgs 0^- resonance (middle); $q\bar{q}$ (85%) and gg (15%) $\rightarrow ZZ$ continuum production (bottom).

Table 19: Results of hypothesis separation for the first $ZZ \rightarrow 4l$ event candidate on CMS showing $\chi^2 = 2\ln(\mathcal{L}_1/\mathcal{L}_2)$ for the eight scenarios with the resonances $ab \rightarrow X \rightarrow ZZ \rightarrow 4l$ and continuum $ab \rightarrow ZZ \rightarrow 4l$ production.

vs.	ZZ	0^+	0^-	1^+	1^-	2_m^+	2_L^+
0^+	-0.36						
0^-	0.09	0.45					
1^+	0.40	0.76	0.31				
1^-	0.47	0.83	0.37	0.64			
2_m^+	-1.09	-0.73	-1.18	-1.49	-1.56		
2_L^+	-2.00	-1.64	-2.09	-2.41	-2.47	-0.92	
2^-	-0.60	-0.24	-0.69	-1.00	-1.06	0.49	1.41

7 Summary and Discussion

In summary, we have proposed to use multivariate likelihood fit which includes five angles and several kinematic variables to determine spin, quantum numbers, and couplings of a $X \rightarrow ZZ$ resonance, and to separate it from background at the same time. This allows one to distinguish between various hypotheses in a model-independent way and to improve separation of signal from background. Certain issues specific to the below-threshold $X \rightarrow ZZ^*$ decay are discussed. The analysis is implemented in `Roofit` which allows combination with other statistical tools developed on CMS and other LHC experiments. In addition to the golden four-lepton final state, we have investigated the semi-leptonic final state with two jets and showed that at higher mass this channel dominates the measurements of the $X \rightarrow ZZ$ decay and both channels allow full angular analysis of the final state.

A dedicated MC program is used to simulate various types of signal including all spin correlations. Detailed MC studies are performed with several bench-mark processes and several mass assumptions. The emphasis is given to the scenario of the first LHC run with 1/fb at 7 TeV center-of-mass energy.

While the presented studies show significant gain of information from the angular analysis in both leptonic and semi-leptonic modes of the $X \rightarrow ZZ$ final state, certain studies specific to yield optimization were left for further studies. In particular certain improvements have been investigated in the semi-leptonic final state, but were left out from this note or were left for later studies:

- Particle Flow jet reconstruction;
- kinematic constraint of the $Z \rightarrow jj$ invariant mass m_{jj} to the mean Z mass m_Z ;
- further optimization of the lepton, jet, and kinematic selection;
- study of the rest-of-the-event observables (MET, high- p_T jets, leptons, etc);
- categorization of the jet flavor type (b , c , light flavor, glue);
- inclusion of new variables in the likelihood fit, and in particular m_{jj} ;
- optimized handling of multiple candidates per event;
- more detailed study of background parameterization with NLO generators and data sidebands;
- detailed study of systematic effects due to object reconstruction and trigger.

Besides study of the SM Higgs, angular information and new semileptonic final state will allow CMS to set limits on (or discover if such particles exist) a wider range of BSM scenarios predicting new states decaying to ZZ final states, such as a spin-1 “heavy photon” A_H in a Little Higgs model or spin-2 RS Graviton in the model with extra dimensions. Some of the best limits on some of the models can be achieved from the di-lepton or di-photon final state. However, there are scenarios where those modes are highly suppressed, as for RS Graviton when light fermions are localized in the bulk of the extra dimension (which solves the flavor problem). The present limit from Tevatron on RS $G \rightarrow ZZ$ is $m_G > 500$ GeV for $c = 0.1$, see Fig. 22. With the first LHC run 1/fb at 7 TeV we can almost double the lower limit to $m_G > 850$ GeV, see Fig. 22. Since the dominant production mechanism of such a graviton is gluon fusion, LHC has an advantage over the Tevatron at higher masses due to higher energy.

8 Acknowledgements

We wish to thank CMS collaboration colleagues for feedback during the regular working group presentations of this analysis, and in particular Nicola De Filippis for regular discussions and support of the four-lepton Higgs analysis package; conveners of the Higgs and Exotica groups (Andrey Korytov, Vivek Sharma, Sarah Eno, Albert De Roeck, Greg Landsberg, Chris Hill) for support and useful discussions; Bob Cousins for discussion of the \mathcal{S} significance estimator. We would also like to thank Yanyan Gao for collaboration during the early stages of this analysis and in particular for contributions to Ref. [10]. Fast simulation and calculations were performed on the Homewood High Performance Cluster of the JHU.

A Angular Formalism

Here the results from Ref. [10] are summarized briefly. The general angular distribution in the production and decay of a spin- J particle X in parton collisions $ab \rightarrow X \rightarrow ZZ \rightarrow (f_1 \bar{f}_1)(f_2 \bar{f}_2)$ is given below. The polarization fractions are defined as follows $f_{\lambda_1 \lambda_2} = |A_{\lambda_1 \lambda_2}|^2 / \sum_{k,l=\pm,0} |A_{kl}|^2$, $\phi_{\lambda_1 \lambda_2} = \arg(A_{\lambda_1 \lambda_2} / A_{00})$, and f_m are the fractions of the initial state spin projection m on the z axis.

$$\begin{aligned}
& \frac{\mathcal{N}_J d\Gamma_J}{\Gamma d\cos\theta^* d\Psi d\cos\theta_1 d\cos\theta_2 d\Phi} = \\
& F_{00}^J(\theta^*) \times \left\{ 4f_{00} \sin^2\theta_1 \sin^2\theta_2 + (f_{++} + f_{--}) \left((1 + \cos^2\theta_1)(1 + \cos^2\theta_2) + 4R_1 R_2 \cos\theta_1 \cos\theta_2 \right) \right. \\
& \quad - 2(f_{++} - f_{--}) (R_1 \cos\theta_1 (1 + \cos^2\theta_2) + R_2 (1 + \cos^2\theta_1) \cos\theta_2) \\
& \quad + 4\sqrt{f_{++}f_{00}} (R_1 - \cos\theta_1) \sin\theta_1 (R_2 - \cos\theta_2) \sin\theta_2 \cos(\Phi + \phi_{++}) \\
& \quad + 4\sqrt{f_{--}f_{00}} (R_1 + \cos\theta_1) \sin\theta_1 (R_2 + \cos\theta_2) \sin\theta_2 \cos(\Phi - \phi_{--}) \\
& \quad \left. + 2\sqrt{f_{++}f_{--}} \sin^2\theta_1 \sin^2\theta_2 \cos(2\Phi + \phi_{++} - \phi_{--}) \right\} \\
& + 4F_{11}^J(\theta^*) \times \left\{ (f_{+0} + f_{0-})(1 - \cos^2\theta_1 \cos^2\theta_2) - (f_{+0} - f_{0-})(R_1 \cos\theta_1 \sin^2\theta_2 + R_2 \sin^2\theta_1 \cos\theta_2) \right. \\
& \quad \left. + 2\sqrt{f_{+0}f_{0-}} \sin\theta_1 \sin\theta_2 (R_1 R_2 - \cos\theta_1 \cos\theta_2) \cos(\Phi + \phi_{+0} - \phi_{0-}) \right\} \\
& + (-1)^J \times 4F_{-11}^J(\theta^*) \times \left\{ (f_{+0} + f_{0-})(R_1 R_2 + \cos\theta_1 \cos\theta_2) - (f_{+0} - f_{0-})(R_1 \cos\theta_2 + R_2 \cos\theta_1) \right. \\
& \quad \left. + 2\sqrt{f_{+0}f_{0-}} \sin\theta_1 \sin\theta_2 \cos(\Phi + \phi_{+0} - \phi_{0-}) \right\} \sin\theta_1 \sin\theta_2 \cos(2\Psi) \\
& + 2F_{22}^J(\theta^*) \times f_{+-} \left\{ (1 + \cos^2\theta_1)(1 + \cos^2\theta_2) - 4R_1 R_2 \cos\theta_1 \cos\theta_2 \right\} \\
& + (-1)^J \times 2F_{-22}^J(\theta^*) \times f_{+-} \sin^2\theta_1 \sin^2\theta_2 \cos(4\Psi) \\
& + 2F_{02}^J(\theta^*) \times \left\{ 2\sqrt{f_{00}f_{+-}} \sin\theta_1 \sin\theta_2 \times \left[(R_1 - \cos\theta_1)(R_2 + \cos\theta_2) \cos(2\Psi - \phi_{+-}) \right. \right. \\
& \quad \left. \left. + (R_1 + \cos\theta_1)(R_2 - \cos\theta_2) \cos(2\Psi + \phi_{+-}) \right] \right. \\
& \quad + \sqrt{f_{++}f_{+-}} \left[\sin^2\theta_1 (1 - 2R_2 \cos\theta_2 + \cos^2\theta_2) \cos(2\Psi - \Phi + \phi_{+-} - \phi_{++}) \right. \\
& \quad \left. + (1 - 2R_1 \cos\theta_1 + \cos^2\theta_1) \sin^2\theta_2 \cos(2\Psi + \Phi - \phi_{+-} + \phi_{++}) \right] \\
& \quad + \sqrt{f_{--}f_{+-}} \left[\sin^2\theta_1 (1 + 2R_2 \cos\theta_2 + \cos^2\theta_2) \cos(2\Psi - \Phi - \phi_{+-} + \phi_{--}) \right. \\
& \quad \left. \left. + (1 + 2R_1 \cos\theta_1 + \cos^2\theta_1) \sin^2\theta_2 \cos(2\Psi + \Phi + \phi_{+-} - \phi_{--}) \right] \right\} \\
& - 2\sqrt{2} F_{01}^J(\theta^*) \times \left\{ 2\sqrt{f_{00}f_{+0}} \left[\sin\theta_1 (R_1 - \cos\theta_1) \sin^2\theta_2 \cos(\Psi - \Phi/2 - \phi_{+0}) \right. \right. \\
& \quad \left. \left. - \sin^2\theta_1 \sin\theta_2 (R_2 - \cos\theta_2) \cos(\Psi + \Phi/2 + \phi_{+0}) \right] \right. \\
& \quad + 2\sqrt{f_{00}f_{0-}} \left[\sin^2\theta_1 \sin\theta_2 (R_2 + \cos\theta_2) \cos(\Psi + \Phi/2 - \phi_{0-}) \right. \\
& \quad \left. \left. - \sin\theta_1 (R_1 + \cos\theta_1) \sin^2\theta_2 \cos(\Psi - \Phi/2 + \phi_{0-}) \right] \right. \\
& \quad \left. + \sqrt{f_{++}f_{+0}} \left[(1 - 2R_1 \cos\theta_1 + \cos^2\theta_1) \sin\theta_2 (R_2 - \cos\theta_2) \cos(\Psi + \Phi/2 + \phi_{++} - \phi_{+0}) \right. \right.
\end{aligned}$$

$$\begin{aligned}
& -\sin\theta_1(R_1 - \cos\theta_1)(1 - 2R_2 \cos\theta_2 + \cos^2\theta_2) \cos(\Psi - \Phi/2 - \phi_{++} + \phi_{+0}) \Big] \\
& + \sqrt{f_{++}f_{0-}} \Big[\sin\theta_1(R_1 - \cos\theta_1) \sin^2\theta_2 \cos(\Psi + 3\Phi/2 + \phi_{++} - \phi_{0-}) \\
& \quad - \sin^2\theta_1 \sin\theta_2(R_2 - \cos\theta_2) \cos(\Psi - 3\Phi/2 - \phi_{++} + \phi_{0-}) \Big] \\
& + \sqrt{f_{--}f_{+0}} \Big[\sin^2\theta_1 \sin\theta_2(R_2 + \cos\theta_2) \cos(\Psi - 3\Phi/2 + \phi_{--} - \phi_{+0}) \\
& \quad - \sin\theta_1(R_1 + \cos\theta_1) \sin^2\theta_2 \cos(\Psi + 3\Phi/2 - \phi_{--} + \phi_{+0}) \Big] \\
& + \sqrt{f_{--}f_{0-}} \Big[\sin\theta_1(R_1 + \cos\theta_1)(1 + 2R_2 \cos\theta_2 + \cos^2\theta_2) \cos(\Psi - \Phi/2 + \phi_{--} - \phi_{0-}) \\
& \quad - (1 + 2R_1 \cos\theta_1 + \cos^2\theta_1) \sin\theta_2(R_2 + \cos\theta_2) \cos(\Psi + \Phi/2 - \phi_{--} + \phi_{0-}) \Big] \Big\} \\
& - 2\sqrt{2} F_{12}^J(\theta^*) \times \Big\{ \sqrt{f_{+-}f_{+0}} \Big[(1 - 2R_1 \cos\theta_1 + \cos^2\theta_1) \sin\theta_2(R_2 + \cos\theta_2) \cos(\Psi + \Phi/2 - \phi_{+-} + \phi_{+0}) \\
& \quad - \sin\theta_1(R_1 + \cos\theta_1)(1 - 2R_2 \cos\theta_2 + \cos^2\theta_2) \cos(\Psi - \Phi/2 + \phi_{+-} - \phi_{+0}) \Big] \\
& + \sqrt{f_{+-}f_{0-}} \Big[\sin\theta_1(R_1 - \cos\theta_1)(1 + 2R_2 \cos\theta_2 + \cos^2\theta_2) \cos(\Psi - \Phi/2 - \phi_{+-} + \phi_{0-}) \\
& \quad - (1 + 2R_1 \cos\theta_1 + \cos^2\theta_1) \sin\theta_2(R_2 - \cos\theta_2) \cos(\Psi + \Phi/2 + \phi_{+-} - \phi_{0-}) \Big] \Big\} \\
& - (-1)^J \times 2\sqrt{2} F_{-12}^J(\theta^*) \times \Big\{ \sqrt{f_{+-}f_{+0}} \Big[\sin\theta_1(R_1 - \cos\theta_1) \sin^2\theta_2 \cos(3\Psi + \Phi/2 - \phi_{+-} + \phi_{+0}) \\
& \quad - \sin^2\theta_1 \sin\theta_2(R_2 - \cos\theta_2) \cos(3\Psi - \Phi/2 + \phi_{+-} - \phi_{+0}) \Big] \\
& + \sqrt{f_{+-}f_{0-}} \Big[\sin^2\theta_1 \sin\theta_2(R_2 + \cos\theta_2) \cos(3\Psi - \Phi/2 - \phi_{+-} + \phi_{0-}) \\
& \quad - \sin\theta_1(R_1 + \cos\theta_1) \sin^2\theta_2 \cos(3\Psi + \Phi/2 + \phi_{+-} - \phi_{0-}) \Big] \Big\}, \tag{6}
\end{aligned}$$

where \mathcal{N}_J is the normalization factor which does not affect the angular distributions and the functions $F_{ij}^J(\theta^*)$ are defined as follows

$$F_{ij}^J(\theta^*) = \sum_{m=0,\pm 1,\pm 2} f_m d_{mi}^J(\theta^*) d_{mj}^J(\theta^*), \tag{7}$$

where $f_{\pm 1} = f_{z1}/2$, $f_{\pm 2} = f_{z2}/2$, and $f_0 = f_{z0} = (1 - f_{z1} - f_{z2})$. Note that for odd J one has $f_{00} = f_{++} = f_{--} = 0$, and therefore $F_{0j}^{J=\text{odd}}(\theta^*)$ terms do not contribute.

For spin-zero, only F_{00}^0 is non-zero and is constant. For spin-one, only $F_{\pm 11}^1 = \frac{1}{4}(1 \pm \cos^2\theta^*)$ are non-zero. For a higher spin, generally all terms contribute.

B Mass Distributions Below the ZZ Threshold

The helicity amplitudes $A_{\lambda_1\lambda_2}$ are good experimental observables in the case of the narrow-mass approximation. This is a good approximation for a narrow resonance X with a mass above the ZZ mass threshold. However, below the ZZ threshold, these amplitudes depend on the actual mass of the two daughters in the decay $X \rightarrow ZZ$. In the example of the spin-zero X particle, its coupling to two Z bosons is generally described as

$$A(X \rightarrow VV) = v^{-1} \epsilon_1^{*\mu} \epsilon_2^{*\nu} \left(a_1 g_{\mu\nu} m_X^2 + a_2 q_\mu q_\nu + a_3 \epsilon_{\mu\nu\alpha\beta} q_1^\alpha q_2^\beta \right), \tag{8}$$

with the three coupling constants a_1 , a_2 , and a_3 which are dimensionless and complex. The helicity amplitudes are calculated as follows

$$A_{00} = -\frac{m_X^2}{v} (a_1 \chi + a_2 \eta (\chi^2 - 1)), \tag{9}$$

$$A_{\pm\pm} = \frac{m_X^2}{v} \left(a_1 \pm \frac{ia_3 \eta \sqrt{\chi^2 - 1}}{2} \right), \tag{10}$$

where the parameters χ and η depend on the masses of the particles, and in particular on the mass m_* of the off-shell Z^*

$$\chi = (m_X^2 - m_Z^2 - m_*^2)/(2m_Z m_*)$$

$$\eta = m_Z M_*/m_X^2, \quad (11)$$

The angular distribution would still be described by Eq. (6), but the values of $f_{\lambda_1 \lambda_2}$ are no longer good quantities to fit for since they are not constant. Instead, $f_{\lambda_1 \lambda_2}$ should be substituted by $|A_{\lambda_1 \lambda_2}|^2$ expressed through coupling constants and masses using Eq. (9). Therefore, the 5D angular distribution becomes 6D mass-angular distribution where dependence on m_* enters in a correlated way.

We define the dimensionless coupling constants $a_i = a_1, a_2, a_3$ as $a_i = |a_i|e^{i\phi_i}$. We can see the dependence of the angular distribution on the off-shell boson mass m_* through η, χ by writing down the free parameters:

$$\begin{aligned} |A_{00}|^2 &= \frac{M_X^4}{v^2} \left\{ |a_1|^2 \chi^2 + |a_2|^2 \eta^2 (\chi^2 - 1)^2 + 2|a_1||a_2|\chi(\chi^2 - 1)\eta \cos(\phi_1 - \phi_2) \right\} \\ |A_{\pm\pm}|^2 &= \frac{M_X^4}{v^2} \left\{ |a_1|^2 + |a_3|^2 \eta^2 (\chi^2 - 1) \pm 2|a_1||a_3|\chi\eta\sqrt{\chi^2 - 1} \cos(\phi_1 - \phi_3) \right\} \\ \phi_{00} &= \arctan 2 \left[\frac{|a_1|\chi \cos \phi_1 + |a_2|\eta(\chi^2 - 1) \cos \phi_2}{|a_1|\chi \sin \phi_1 + |a_2|\eta(\chi^2 - 1) \sin \phi_2} \right] \\ \phi_{\pm\pm} &= \arctan 2 \left[\frac{|a_1| \cos \phi_1 \mp |a_3|\eta\sqrt{\chi^2 - 1} \cos \phi_3}{|a_1| \sin \phi_1 \pm |a_3|\eta\sqrt{\chi^2 - 1} \sin \phi_3} \right] \end{aligned} \quad (12)$$

To write down the fully differential mass-angle expression, we must add in the Z^* propagator term, as in Eq. (23) of Ref. [36].

$$\frac{d\Gamma_{J=0}}{\Gamma dM_* d\cos\theta_1 d\cos\theta_2 d\Phi} \propto \frac{M_*^3 \beta}{(M_*^2 - M_Z^2)^2 + M_Z^2 \Gamma_Z^2} \left[\frac{d\Gamma_{J=0}}{\Gamma d\cos\theta_1 d\cos\theta_2 d\Phi}(M_*, \cos\theta_1, \cos\theta_2, \Phi) \right] \quad (13)$$

where we have defined:

$$\beta^2 = \left[1 - \frac{(M_Z + M_*)^2}{M_X^2} \right] \left[1 - \frac{(M_Z - M_*)^2}{M_X^2} \right] \quad (14)$$

As a cross-check, in Fig. 28 we show the invariant mass distribution for the virtual Z^* by integrating out the angular contribution for the case of a scalar and pseudoscalar spin-zero particle at 140 GeV. This is equivalently the distribution of $(|A_{++}|^2 + |A_{--}|^2 + |A_{00}|^2)$ with the mass dependence expressed through Eq. (9). For the case of a scalar spin-zero, we set $a_1 = 1$ and $a_2 = a_3 = \phi_i = 0$. For the case of a pseudoscalar spin-zero, we set $a_3 = 1$ and $a_1 = a_2 = \phi_i = 0$. The results in Fig. 28 does not appear to be identical to Fig. 11 of Ref. [37], but we note that we plot $d\Gamma/dM_*$ vs M_* , while there is confusion in the literature due to plotting $d\Gamma/dM_*^2$ vs M_* , which becomes misleading as for example Fig. 3 in Ref. [36].

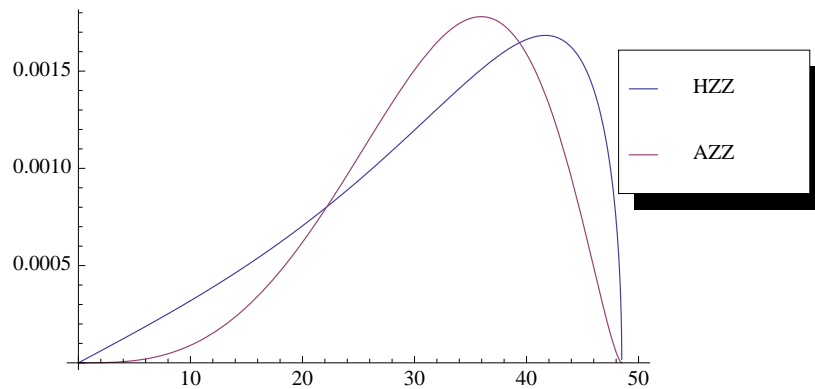


Figure 28: 1D distribution of the virtual Z invariant mass, m_* , for a scalar and pseudoscalar spin-zero particle.

References

- [1] The LEP Electroweak Working Group and the Tevatron Electroweak Working Group, <http://lepewwg.web.cern.ch/LEPEWWG/>

- [2] A. Soni and R. M. Xu, Phys. Rev. D **48**, 5259 (1993).
- [3] B. C. Allanach *et al.*, “Exploring Small Extra Dimensions at the Large Hadron Collider,” JHEP 0212, 039 (2002).
- [4] S.Y. Choi, D. J. Miller, M.M. Muhlleitner, and P. M. Zerwas, Phys. Lett. B **553**, 61 (2003).
- [5] C.P. Buszello, I. Fleck, P. Marquard, and J.J. van der Bij, Eur. Phys. J. C **32**, 209 (2004).
- [6] R. M. Godbole, D. J. . Miller and M. M. Muhlleitner, “Aspects of CP violation in the H ZZ coupling at the LHC,” JHEP **0712**, 031 (2007).
- [7] W. Y. Keung, I. Low, and J. Shu, Phys. Rev. Lett. **101**, 091802 (2008).
- [8] O. Antipin and A. Soni, JHEP **0810**, 018 (2008).
- [9] K. Hagiwara, Q. Li, and K. Mawatari, ”Jet angular correlation in vector-boson fusion processes at hadron colliders,” JHEP **07**, 101 (2009).
- [10] Y.Y. Gao *et al.*, Phys. Rev. D **81**, 075022 (2010).
- [11] A. De Rujula *et al.*, arXiv:1001.5300 [hep-ph].
- [12] T. L. Trueman, Phys. Rev. D **18**, 3423 (1978).
- [13] J. R. Della’Aquila and C. A. Nelson, Phys. Rev. D **33**, 80 (1986).
- [14] V. Barger, Y. Gao, W.-Y. Keung, “T-Anomaly Induced LHC Signals,” Phys. Lett. B **655**, 228 (2007).
- [15] J. E. Juknevich, D. Melnikov, and M. J. Strassler, JHEP **0907**, 055 (2009).
- [16] L. Randall, R. Sundrum, Phys. Rev. Lett. **83** (1999) 3370 and *ibid* (1999) 4690.
- [17] K. Agashe, H. Davoudiasl, G. Perez and A. Soni, Phys. Rev. D **76** (2007) 036006 [arXiv:hep-ph/0701186].
- [18] CMS Collaboration, “Search for Randall-Sundrum Gravitons in the Diphoton Final State,” CMS PAS EXO-09-009.
- [19] CMS Collaboration, “Search for High Mass Resonances Decaying into an Electron Pair in CMS at 10 TeV with 100 pb⁻¹,” CMS PAS EXO-09-006.
- [20] CMS Collaboration, “Search for New High-Mass Resonances Decaying to Muon Pairs in the CMS Experiment,” CMS PAS SBM-07-002.
- [21] CMS Collaboration, “Search for High-Mass Resonances Decaying into Top-Antitop Pairs in the All-Hadronic Mode,” CMS PAS EXO-09-002.
- [22] CDF collaboration, “Search for $X \rightarrow ZZ$ with 3/fb and Forward Tracking,” CDF-note-9640 (2009).
- [23] Fabian Stockli and Rebeca Gonzalez Suarez, for the CMS Higgs Working-Group, “SM Higgs Production Cross-Section and Branching-Ratios at 10 TeV and 7 TeV,” <http://www.cern.ch/HiggsCrossSections/> revision February 9, 2010. For later updates (not used in this version), see <https://twiki.cern.ch/twiki/bin/view/LHCPhysics/CrossSectionsCalc>
- [24] For generator documentation, see documentation at <http://www.pha.jhu.edu/spin/> and Ref. [10]. Simulation was performed on the Homewood High Performance Cluster of the JHU.
- [25] Pythia generator package, <http://home.thep.lu.se/~torbjorn/Pythia.html>
- [26] S. Baffioni, *et al.*, ”Search strategy for the Higgs boson in the $ZZ^{(*)}$ decay channel with the CMS experiment,” CMS AN 2008/050.
- [27] S. Baffioni, *et al.*, ”Search strategy for the Higgs boson in the $ZZ^{(*)}$ decay channel at $\sqrt{s} = 10$ TeV with the CMS experiment,” CMS AN 2010/237.
- [28] CMS Collaboration ”Search strategy for the Higgs boson in the $ZZ^{(*)}$ decay channel with the CMS experiment,” CMS PAS HIG-08-003.

- [29] See <https://twiki.cern.ch/twiki/bin/view/CMS/HiggsZZMCsamples7TeV> and <https://twiki.cern.ch/twiki/bin/viewauth/CMS/StandardModelCrossSections>
- [30] MadGraph generator package, <http://madgraph.hep.uiuc.edu/index.html>
- [31] T. Binoth, N. Kauer, and P. Mertsch, “Gluon-induced QCD corrections to $pp \rightarrow ZZ \rightarrow l \text{ anti-}l'$,” arXiv:0807.0024 [hep-ph]; and “GG2ZZ parton-level integrator and event generator,” <http://hepsource.sourceforge.net/programs/GG2ZZ/>
- [32] “Physics Analysis Toolkit (PAT),” <https://twiki.cern.ch/twiki/bin/view/CMS/SWGuidePAT>
- [33] Particle Data Group, “Review of particle physics,” Phys. Lett. B **667**, 1 (2008).
- [34] F. James *et al.*, MINUIT, “Function minimization and error analysis CERN program library;” R. Brun *et al.*, “Root data-analysis framework;” and D. Kirkby *et al.*, “The RooFit toolkit for data modeling,” <http://root.cern.ch/>.
- [35] R. Cousins, J. Mumford, J. Tucker, and V. Valuev, JHEP **11**, 046 (2005).
- [36] S. Y. Choi, D. J. Miller, M. M. Muhlleitner, and P. M. Zerwas, Phys. Lett. B 553, 61 (2003).
- [37] V. Barger *et al.*, Phys. Rev D. 49, 79 (1994).